Locked up Inside the Vessels: Rare Earth Elements Are Transferred and Stored in the Conductive Tissues of the Accumulating Fern Dryopteris erythrosora

Marie Le Jean, Emmanuelle Montargès-Pelletier, Camille Rivard, Nicolas Grosjean, Michel Chalot, Delphine Vantelon, Kathryn Spiers, Damien Blaudez

Locked up inside the vessels: Rare earth elements are transferred and stored in the conductive tissues of the accumulating fern *Dryopteris erythrosora*

Marie Le Jean[a]*, Emmanuelle Montargès-Pelletier[b], Camille Rivard[c,d], Nicolas Grosjean[a,b,†], Michel Chalot[e,f], Delphine Vantelon[c], Kathryn M. Spiers[g], Damien Blaudez[b]

[a]*Université de Lorraine, CNRS, LIEC, F-57000 Metz, France*

[b]*Université de Lorraine, CNRS, LIEC, F-54000 Nancy, France*

[c]*Synchrotron SOLEIL, F-91190 Saint-Aubin, France*

[d]*INRAE, TRANSFORM, F-44300 Nantes, France*

[e]*Université de Franche-Comté, CNRS, Laboratoire Chrono-Environnement, F-25000 Besançon, France*

[f]*Université de Lorraine, F-54000 Nancy, France*

[g]*Deutsches Elektronen-Synchrotron DESY, D-22607 Hamburg, Germany*

*Corresponding author:

Dr Marie Le Jean

E-mail: marie.lejean@univ-lorraine.fr

ABSTRACT

Rare earth elements (REEs) are strategic metals strongly involved in low-carbon energy conversion. However, these emerging contaminants are increasingly disseminated into ecosystems, raising concern regarding their toxicity. REE-accumulating plants are crucial subjects to better understand REE transfer to the trophic chain but are also promising phytoremediation tools. In this analysis, we deciphered REE accumulation sites in the REE-accumulating fern *Dryopteris erythrosora* by synchrotron X-ray μfluorescence (μXRF). This technique allows a high-resolution and *in situ* analysis of fresh samples or frozen-hydrated cross sections of different organs of the plant. In the sporophyte, REEs were translocated from the roots to the fronds by the xylem sap and were stored within the xylem conductive system. The comparison of REE distribution and accumulation levels in the healthy and necrotic parts of the frond shed light on the differential mobility between light and heavy REEs. Furthermore, the comparison emphasized that necrotized areas were not the main REE-accumulating sites. Finally, the absence of cell-to-cell mobility of REEs in the gametophyte suggested the absence of REE-compatible transporters in photosynthetic tissues. These results provide valuable knowledge on the physiology of REE-accumulating ferns to understand the REE cycle in biological systems and the expansion of phytotechnologies for REE-enriched or -contaminated soils.

KEYWORDS

Lanthanides, accumulating ferns, conductive vessels, phytoremediation, X-ray microfluorescence.

SYNOPSIS

This study reveals the accumulation sites in a model of accumulating ferns for light and heavy rare earth elements, emerging metal contaminants in the environment.

INTRODUCTION

The high-demand technological elements known as rare earth elements (REEs) include the 15 lanthanides plus yttrium (Y) and scandium (Sc) as defined by the International Union of Pure and Applied Chemistry[1]. According to their atomic mass, REEs can be split into light REEs (LREEs from lanthanum (La) to europium (Eu) plus Sc) and heavy REEs (HREEs, from gadolinium (Gd) to lutetium (Lu) plus Y)[2]. Their physicochemical properties make REEs essential for numerous and multifaceted domains, such as green energy, industry high technologies and medicine[3]. REE-containing substrates such as lanthanum-modified bentonite (LMB) are also used in water eutrophication remediation[4], even if adverse effects such as a reduced bioavailable phosphorus and formed anaerobic horizon from LMB may be harmful to submerged macrophytes[5]. REEs are also used to increase productivity in agriculture and livestock farming[6]. Consequently, REE mining, intense utilization associated with low recyclability[7], is responsible for an ever increasing contamination of the soils and waters. For instance, hospitals are responsible for high anthropogenic Gd anomalies in rivers and estuarine waters[8,9]. Additionally, REE concentrations can reach up to 2000-27000 mg kg^{-1} in soils from mining areas[10], whereas the average worldwide soil concentration ranges from 100 to 200 mg kg^{-1} [11]. The use of REEs as fertilizers to increase yield in Chinese agriculture during the last decades have also contributed to REE spreading in the soils and surface waters[12]. Although most countries do not specifically apply REEs to crops, the wide usage of phosphate fertilizers

66 enriched with REEs also represents an unintentional source of REE pollution[10,13]. For instance,
67 the concentration of REEs in single superphosphate (SSP) varies from 500 to 8,300 mg kg^{-1},
68 making its use as fertilizer a major REE source of 23,800 tons of REEs spread in Brazil in
69 2014[10,13].

70 When applied at low concentrations, REEs trigger hormetic effects in various organisms[14,15],
71 thereby justifying their use in agriculture as fertilizers[13,16]. However, the beneficial effects of
72 low-dose application of cerium to crops is challenged in a recent meta-analysis[17], questioning the
73 aim to increase yield at the expense of the ecosystem quality. Nevertheless, their noxiousness at
74 high concentrations is now well established[11,15,17,18]. The biological effects of REEs are now
75 considered a major emerging environmental issue, as these elements are taken up by living
76 organisms in contaminated ecosystems and induce toxic effects, with a higher toxicity for
77 HREEs over LREEs[11,15,19–2220,21].

78 Metal/metalloid accumulating plants are valuable tools to remove metallic pollutants from
79 contaminated areas. These plants can be used for ecosystem restoration by phytoremediation but
80 can also be considered a profitable resource for agromining[23,24]. REE-accumulating plants exist
81 among diverse euphyllophyta groups, with the class polypodiopsida (ferns) being the most
82 represented[25,26] plus the two mesangiosperm genera *Phytolacca*[27,28] and *Carya*[29]. Interestingly,
83 ferns preferentially accumulate LREEs, whereas angiosperms store more HREEs [30–32]. This
84 discrepancy might reflect the onset of distinct REE absorption and transfer strategies throughout
85 evolution.

86 Unraveling the transfer and storage mechanisms of REEs in these plants is of utmost importance
87 to understand metal transfer to the biota. Furthermore, this will ensure proper selection of the

88 best candidates for either phytoremediation or agromining, depending on the pollution context.
89 The distribution of REEs within the accumulating ferns *Dicranopteris linearis, Pronephrium*
90 *simplex* and *Dryopteris erythrosora* was first investigated either by tissue fractionation
91 techniques or using radioactive tracers, showing that REEs were stored in the chloroplasts for the
92 three species, in the cell walls for the first two [33–35], and at the tip of the pinnae with no staining
93 along the veins for the latter[25]. The experimental biases of this methodology (tissue fractionation,
94 loss of root integrity during REE radioactive tracer use and indirect REE detection) urged more
95 accurate, nondestructive and direct detection analysis provided by synchrotron μXRF. Recently,
96 the *in planta* distribution of REEs has been reported for *D. linearis*[31]. These experiments on fresh
97 tissues notably showed that most of the REEs detected (mainly La and Ce) were stored in the
98 epidermis of the fronds and to a lesser extent in the conductive tissues of the fronds. However,
99 the distribution of HREEs was not determined, likely due to the LREE prevalence in the native
100 soil where these fronds had grown.

101 If *D. linearis and P. simplex* present a high REE accumulation potential, they are subordinate to
102 very specific climates[35] and are also sensitive to microclimate and soil factors[36]. To our
103 knowledge, the publications concerning these ferns only mention naturally occurring plants and
104 never refer to intentional cultivation. These cultivation condition restrictions, notably to sub-
105 tropical rain forests, may constitute a drawback in the context of phytoremediation or
106 agromining, if the REE-contaminated site is under a temperate or cold climate, under which
107 these plants would hardly grow. Therefore, the other REE-accumulating fern, *D. erythrosora*,
108 first identified on noncontaminated soil[26] represents an interesting alternative due to its easy
109 cultivability, hardiness (growth under cold climates) and capacity to preferentially accumulate
110 LREEs[30], the most widespread REEs [11]. Our main objective was therefore to unravel the precise

distribution of LREEs and HREEs in this promising REE-accumulating species. Here, we present the *in situ* μXRF analysis of frond samples and thin frozen cross sections of the different organs of *D. erythrosora*. The environmental profile of REEs in soils is usually enriched in LREEs over HREEs. Given that most environmental studies dealing with REE accumulation in plants are performed *in situ* with soils harboring a general high natural prevalence of LREEs[29,31,37], such systems do not allow adequate comparison of the plants coping with light *versus* heavy REEs in terms of uptake, fractionation and distribution patterns. To avoid this drawback, we used plants grown on a soil spiked with equal concentrations of selected REEs to circumvent a LREE-favored exposure as found in environmental soils. Given the chemical similarities between LREEs and HREEs, we hypothesized that LREEs and HREEs would be distributed similarly in fern tissues. We also hypothesized that the distribution pattern of REEs would differ from that of macronutrients but would remain the same regardless of the concentration of REEs found in tissues. The comparison of REE cellular localization with elements that have contrasted redistribution/mobility potentials, such as Ca, Mn and K, provided insights about the REE mobility in plants. Additionally, the use of different culture conditions and the investigation of two developmental stages strengthened our findings. This study revealed that the REE distribution is associated mostly with conductive vessels, a pattern different from the pattern reported for *D. linearis*, suggesting the existence of different strategies in REE-accumulating ferns to cope with excess REEs.

MATERIALS AND METHODS

Plant culture and growth conditions

The REE-accumulating fern *Dryopteris erythrosora* was used in the present study. Grown plants and fern spores were purchased from 'Les Jardins d'écoute s'il pleut', a nursery specializing in hardy ferns (Saint Michel Le Cloucq, France). Hardy ferns are plant resistant to cold temperatures (down to -15°C), moderate drought and wind. The two developmental stages (sporophyte and gametophyte) were studied. Sporophytes (fern plants) werecultivated in soil and hydroponics, while gametophytes were grown *in vitro*. The gametophyte develops after spore germination, as a small single-cell-thick blade harboring rhizoids (Figure S11A) and on which the gametes are produced and the sexual reproduction occurs.

For the cultivation of ferns on soil, plants were first cleaned from their growing substrate and subsequently transferred to an REE-spiked soil consisting of a Neoluvisol (horizon E) collected in the Forêt de Haye (Vandoeuvre-les-Nancy, France, physicochemical characteristics in Table S1). Hydrated salts of $LaCl_3$, $CeCl_3$, $SmCl_3$, $GdCl_3$ and $YbCl_3$ (Sigma Aldrich, Saint-Quentin-Fallavier, France) were used to spike the soil with an equivalent quantity (83 or 333 mg kg^{-1} dry weight (DW) of each REE (La, Ce, Sm, Gd and Yb) as indicated. The experimental strategy aimed at using only five representatives and comparing light and heavy REEs, added in the culture growth with equal concentrations. Then, we focused on five REEs, with La, Ce and Sm representing LREEs and Gd and Yb representing HREEs. These conditions cannot be reached with natural soils as LREEs commonly dominate the group of REES (about 87%). Chloride salts were used to enhance the bioavailability of REEs, bioavailability was estimated through $CaCl_2$ extraction before REE spiking and at harvest (see supplementary information). The two concentrations of REEs added in this study will thereafter be referred to as medium (415 mg kg^{-1} REEs added) and high (1665 mg kg^{-1} REEs added) REE conditions. An REE solution was sprayed several times onto thin layers of soil (1 cm), and thorough hand mixing was performed

to ensure proper homogenization of the contamination. The REE-spiked soil was finally placed into 3.4-L plastic pots (20 cm × 15 cm × 15 cm) and watered twice a week with deionized water. The aboveground biomass was harvested after two months of exposure.

Details related to the cultivation of ferns in hydroponics, cultivation of gametophytes, elemental analyses of fern tissues, and photonic microscopy observations are given in the Supplemental Text.

For both pot and hydroponic cultures, plants were grown under controlled conditions in a growth chamber (18/23 °C; 8/16 h dark/light cycles; 260 μmol m^{-2} s^{-1}).

Preparation of samples for synchrotron measurements

For the preparation of fresh samples, entire plants were brought to synchrotron facilities, and live samples were prepared on-site immediately prior to scanning to prevent dehydration phenomena. The samples were hand cut with a stainless-steel razor blade ('dry knife'), immediately placed on the 3D printed sample holder, and mounted between two layers of Ultralene (SPEX SamplePrep; 4 μm). Analyses were conducted at room temperature. At least three biological replicates were analyzed and representative samples are shown in the results and in the supporting information.

For the preparation of frozen thin sections, fragments of fern organs were collected from fresh plants and immediately immersed in a water soluble–embedding compound (OCT from VWR, Rosny-sous-Bois, France) and frozen in isopentane cooled by liquid N_2, as described in Castillo-Michel et al. (2017)[38]. Transverse sections of roots, rachis and pinnae were cryosectioned at a thickness of 60 μm using a cryomicrotome (Thermo Fisher Scientific, Illkirch, France) available

at the SOLEIL facility. The thin sections were placed between two Ultralene films in a copper sample holder under freezing conditions at all times.

MicroXRF analyses

The X-ray fluorescence microscopy experiments on fresh samples were undertaken at beamline P06 at PETRA III at DESY (Deutsches Elektronen-Synchrotron, Hamburg, Germany)[39]. The undulator beam was monochromatized with a cryogenically cooled Si(111) channel-cut monochromator to an energy of 11 keV with an X-ray flux on the order of 10^{10} photons s^{-1} [40]. A Kirkpatrick-Baez mirror pair was used to focus the incident beam to 700 nm * 530 nm (h * v). X-ray detection was performed using the Maia detector of the P06 beamline[41, 42], which uses a large detector array to maximize the detected signal and count rates. A quick 'survey scan-overview scan' (50-100 µm with a dwell time of 1-2 ms, taking 5-10 min in total) was first conducted to select the precise area to be scanned. Then, a 'high resolution scan' was conducted (resolution of 2-10 µm and a dwell time of 8-20 ms). Considering that radiation damage might occur above X-ray dose limits of 4.1 kGy [43,44] we used fast scanning (per-pixel dwell time ranging between 1 and 20 ms).

Cryogenic microXRF analyses on thin sections were conducted on the LUCIA beamline[45,46] at SOLEIL synchrotron (Gif-sur-Yvette, France)[46] using the water-cooled fixed exit double-crystal Si(111) monochromator. Micro-XRF elemental maps were collected at 7,300 eV with a beam focused to 3.5 * 3.0 (v × h) μm^2 by means of a Kirkpatrick-Baez mirror arrangement. The XRF signal was collected using a 60 mm^2 silicon drift diode Bruker detector. The pixel size was 15 × 15 μm^2 for the low spatial resolution maps and 3 × 3 μm^2 for the high spatial resolution maps with integration times of 100 and 500 ms per pixel, respectively. The experimental chamber was

operated under vacuum to minimize absorption and scattering by air, and a liquid N_2 cryostat was used. The thin sections were transferred under N_2 vapor into the experimental chamber to maintain the cold chain. Frozen hydrated sections from three to six biological replicates were analyzed, representative samples are shown in the results and the supporting informations.

XRF data treatment

P06 data – The XRF event stream was analyzed using the DynamicAnalysis method[47,48], as implemented in GeoPIXE[49,50]. GeoPIXE provides quantitative first-order self-absorption corrected maps of projected areal elemental density – maps of elemental content (in % or mg kg^{-1}). Conversion of X-ray counts to concentration was performed through analysis of reference foil scans. The samples were each considered to have a uniform thickness (300 μm). The matrix file used for the spectral fitting was an assumed composition of $C_{7.3}O_{33}H_{59}N_{0.7}S_{0.8}$ with a density of 0.90 g cm^{-3} and considering two layers of Ultralene (4 µm) (Figure S1).

LUCIA data – To optimize the discrimination of the various XRF line contributions, the XRF signal of each element was extracted by batch fitting the XRF spectrum in each pixel of the map using PyMCA software[51] (Figure S2). The count number for the XRF signal was normalized by the count number of the incoming beam signal and corrected by the XRF detector deadtime. Three color RGB (red–green-blue) maps were generated to display spatial correlation using Fiji software[52].

RESULTS AND DISCUSSION

Accumulation levels of rare earth elements in fronds of *Dryopteris erythrosora*

218 The total REE concentration of the natural soil used in this study before REE addition (Table S1)
219 was 217.4 mg kg^{-1}, with >86% LREEs, >7% Sc and Y and <6% HREEs. Ce, La, Nd and Y were
220 the four most represented REEs, constituting >87% of REEs. We further focused on five REEs,
221 with La, Ce and Sm representing LREEs and Gd and Yb representing HREEs. Among these
222 REEs, although La and Ce were the two most abundant (33.5 and 115 mg kg^{-1}, respectively),
223 their $CaCl_2$ extractability was low (0.112 and 0.302 mg kg^{-1}, representing each 0.3%,
224 respectively). Samarium and Gd were less abundant but showed a comparable extractability
225 (5.13 and 5.41 mg kg^{-1} in total with 0.4 and 0.5% extractability, respectively), while Yb was less
226 abundant (1.02 mg kg^{-1}) but exhibited a higher extractability (1.6%). Plants grown in this soil
227 accumulated LREEs moderately and HREEs very faintly in their fronds (Table S2). Thus, the
228 discrepancy in LREE and HREE content and availability of the soil impedes their homogeneous
229 accumulation in the fronds and might prevent the detection of low-concentration REEs *in planta*.
230 To increase the total REE content of this soil and to reduce the content gap between LREEs and
231 HREEs, we spiked this natural soil with equivalent amounts of the five REEs selected, namely,
232 medium and high REE contamination (see the Materials and Methods section for details) and
233 transferred *D. erythrosora* plants to these conditions for two months. The REE concentrations
234 used were chosen to reflect a high level of contamination, as can be found in situ[10], and in
235 accordance with previously published work, in which *D. erythrosora* was shown to accumulate
236 more REEs than the other ferns. The $CaCl_2$-extractible fraction of REEs was analyzed under the
237 two conditions (Figure 1A) and revealed an overall increase in the $CaCl_2$ extractible REEs
238 (Figure 1A) under the two conditions. The $CaCl_2$ extractible concentrations of both the selected
239 LREEs and HREEs were in a much closer range than in the natural soil (2-4.81 mg kg^{-1} for
240 medium contamination and 34-56.2 mg kg^{-1} for high contamination), thereby fulfilling our goal.

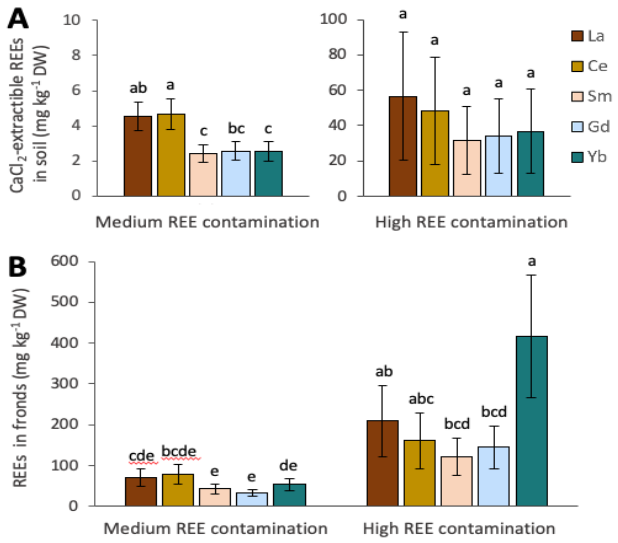

Figure 1. REE concentrations in the $CaCl_2$ extractable fraction of the contaminated soil and in fronds of *Dryopteris erythrosora*. (A) $CaCl_2$-extractable fraction of the five REEs under the two conditions. (B) Concentrations in plants grown on a soil spiked with a medium (83 mg kg^{-1} DW each) or a high level (333 mg kg^{-1} DW each) equimolar mix of La, Ce, Sm, Gd and Yb. For A and B, n=3, mean ± standard deviation (SD). Different letters denote significant differences ($P< 0.05$, analysis of variance (ANOVA)).

Then, the accumulation of the five selected REEs was measured by inductively coupled plasma mass spectrometry (ICP-MS) in fronds of *D. erythrosora*. For the medium contamination condition, a total of 279 mg REEs kg^{-1} DW was found in the fronds (Figure 1B). The five REEs were found at a similar order of magnitude, with 33.2 to 79.1 mg kg^{-1} each, with Sm and Gd slightly less accumulated (Figure 1B). For the high contamination condition, the five REEs were overall 3.8 times more accumulated (1,052 mg kg^{-1}) in the fronds in comparison to the medium contamination (279 mg kg^{-1}). Again, the five REEs in the fronds of this high contamination condition were accumulated at a similar order of magnitude (200-400 mg kg^{-1}). This finding reflects the higher available pool of REEs in the soil solution under high REE conditions. However, the increase in REE accumulation in fronds obtained under the highest REE exposure

(3.8 times) does not follow the increase in the $CaCl_2$-extractible fraction in soils (12 times). The discrepancies observed might result from a limited root-to-shoot transfer; therefore, the accumulation in fronds would not fully represent the available fraction of REEs. It is also possible that $CaCl_2$ extraction does not entirely represent the total available pool of these metals in this type of soil. Despite this, the comparable concentrations of LREEs and HREEs in the fronds measured here were a prerequisite to enable the comparative distribution of the two groups of REEs, as presented thereafter.

REEs are essentially accumulated in the conductive tissues of fronds

To investigate the overall distribution and storage sites of the different REEs, we first performed a μXRF analysis of the whole surface of fresh pinnae (Figure S3) from plants grown under high-REE conditions. As shown in Figure 2A, the distribution of La, Ce, Sm, Gd and Yb overlapped mainly with the vascular pattern of the pinna, and the necrotic tip of the pinna is further described in a dedicated section below. This REE distribution is peculiar when compared to other elements, such as Mn, Ca and K, that are more widely distributed throughout the limb. The distribution pattern of REEs is further illustrated by a good correlation between REEs, e.g., La and Ce distribution over the pinna (Figure 2B), but a weaker correlation between La and Mn. The limited correlation between REEs and Mn could be explained by the presence of Mn-enriched spots in the limb in addition to the veins, while REEs are restricted mostly to the latter. Given the similar ionic radii and affinity to protein binding sites between REEs and Ca[53,54], it has been long hypothesized that these elements could share common transport pathways. However, REEs display a distribution very distinct from that of Ca, suggesting that REEs cannot be redistributed to the limb, either due the absence of REE unloading systems or REE complexation in the vasculature.

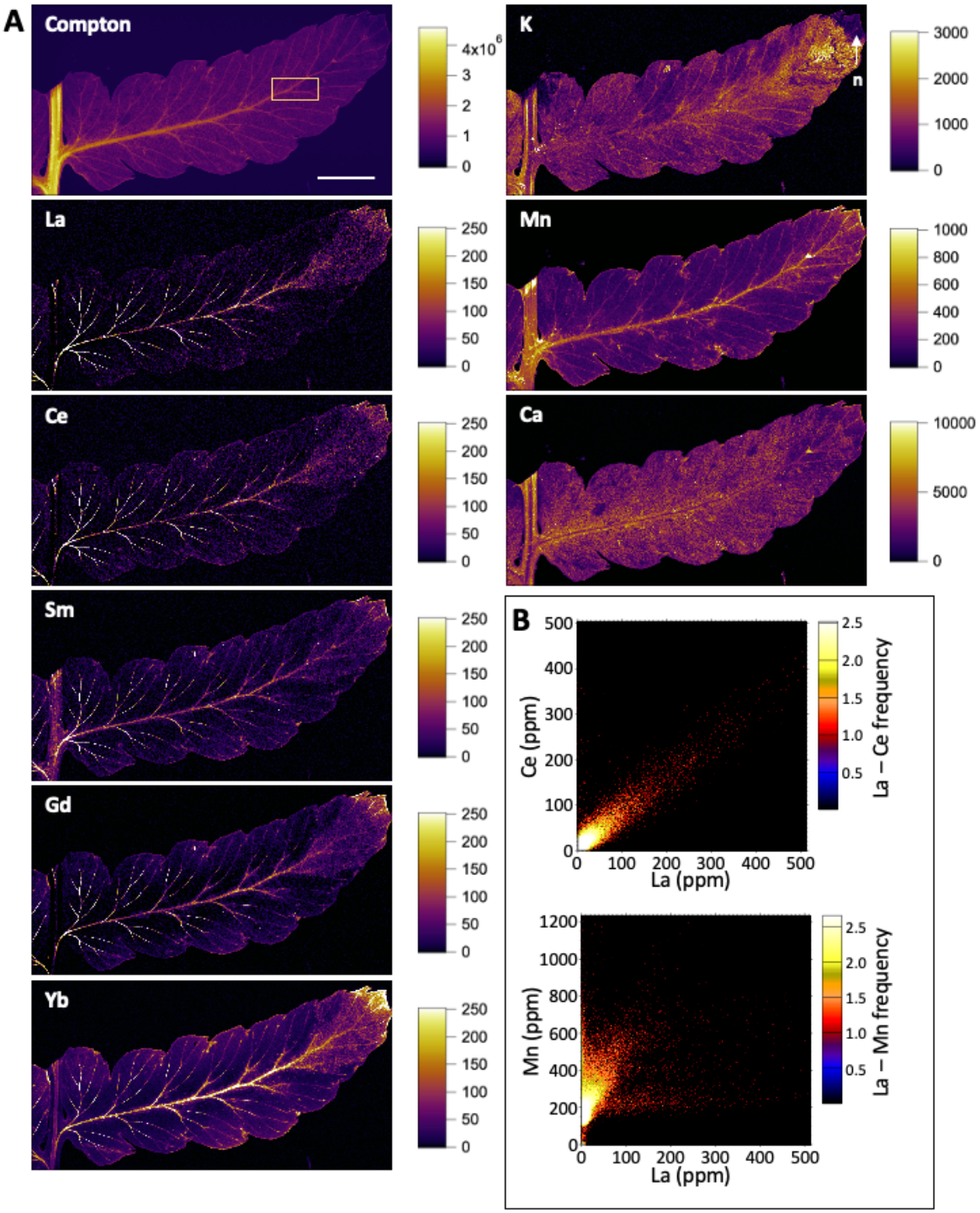

Figure 2. REE distribution in pinnules of *Dryopteris erythrosora*. (A) Synchrotron-based X-ray fluorescence Compton and elemental maps of a fresh *D. erythrosora* pinnule grown on a soil supplemented with equal amounts (333 mg kg^{-1} DW each) of La, Ce, Sm, Gd and Yb. The images of this representative sample were acquired with a step size of 50 μm and a dwell time of 12 ms per pixel. The squared area on the Compton map corresponds to the high-resolution maps shown in Figure 3. The scale bar represents 3 mm. n: necrotic area. The color scale is a quantitative scale in mg/kg except for Compton (number of counts). (B) Correlation charts comparing distributions of La with Ce or Mn. The color scale of correlation graphs reports the frequency of the values on the whole image.

To probe the different REE concentration ranges found in the aboveground biomass of various plants grown worldwide in REE-contaminated soils or REE natural background[11,55–58], we analyzed the REE accumulation sites between plants grown under different conditions. Contrasted REE plant concentrations were measured under these different conditions, namely, medium (279 mg REE kg^{-1} DW in fronds, Figure S4B) and high REE (1,052 mg kg^{-1} in fronds, Figure 2). In parallel, plants with lower amounts of La and Yb in their fronds were obtained through hydroponic cultures (20.1 and 8.02 mg kg^{-1} in fronds of La and Yb, respectively, data not shown). This culture system ensures high REE availability to the roots, while short-term exposure allowed low REE content in the fronds. µXRF analyses revealed a similar pattern of REE localization in the veins of fronds regardless of the accumulation and growing conditions (Figure 2, Figure S4A, B). This finding demonstrates that REE localization in the vasculature of this fern species does not depend on the concentration of REEs in fronds or on the culture system used. Therefore, the hypothesis of the REE restricted mobility is favored, unlike other elements that localize differently depending on the concentration. For instance, Cd and Zn localize to the trichomes of *Arabidopsis halleri* under moderate concentrations and spread to mesophyll cells under high exposure[59].

A high-resolution map (Figure 3) of the squared area in Figure 2A revealed subtle differences between REEs. LREEs showed a rather homogeneous layout at the veins, while HREEs were more unevenly distributed, with a more intense signal at the periphery of the veins. The correlation charts focusing on the squared area in Figure 3 (Figure S5) further strengthened these observations. There was a high correlation between the distribution of REEs of similar ionic radii (e.g., for the two LREEs La-Ce or the two HREEs Yb-Gd) and a lower correlation for REEs with contrasting ionic radii (e.g., LREE *vs* HREE such as La-Gd or La-Yb), especially for the higher

297 concentrations. Thus, LREEs and HREEs appear to share an overall vascular distribution, with
298 subtle differences supporting dissimilar interactions with plant tissues and/or transporters
299 depending on the REE group. Additionally, our results suggest that although a common mode of
300 transport could be shared among REEs and some macronutrients from the soil solution to the
301 aboveground parts of the plant, REEs could not, or could hardly, be unloaded from the
302 vasculature.

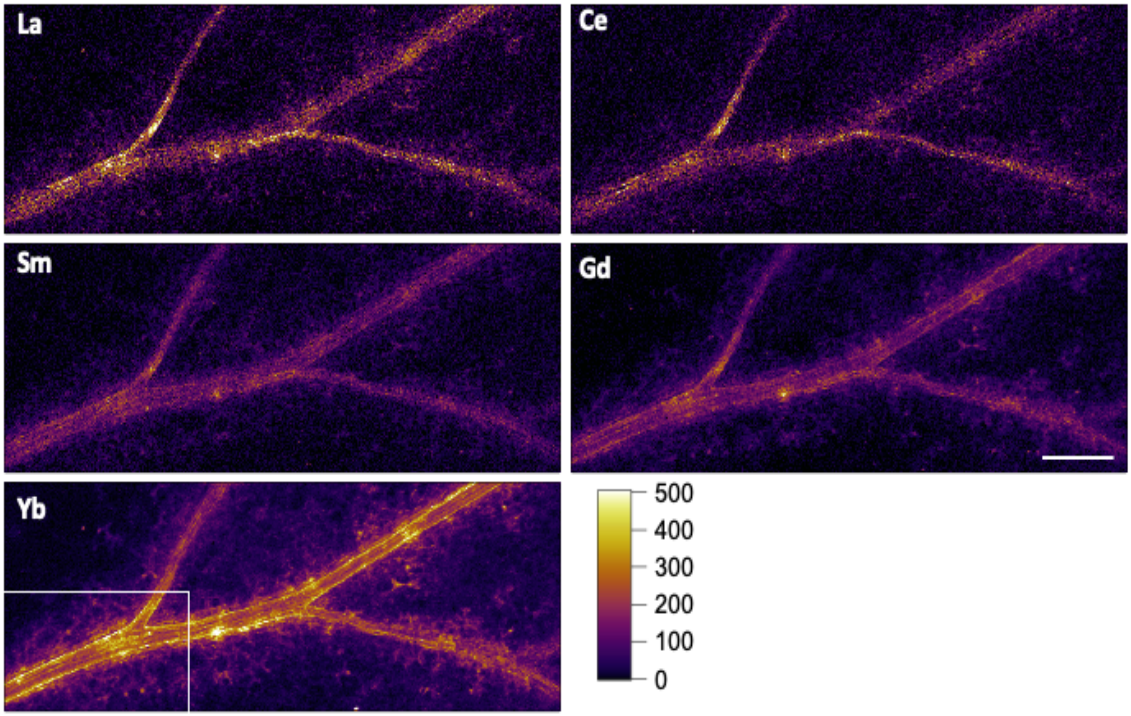

Figure 3. Focus on REE distribution in the vasculature of a pinnule of *Dryopteris erythrosora*. X-ray fluorescence elemental maps were obtained from the zoomed area shown in Figure 2. Same legend as in Figure 2, except that the images of this representative sample were acquired with a step size of 5 μm and a dwell time of 5 ms per pixel. The scale bar represents 300 μm. The color scale is a quantitative scale in mg kg^{-1}. All the maps were uniformly scaled from 0 to 500 mg kg^{-1} as a maximum. The two-element correlation plots are presented in Figure S5.

303

REEs are locked inside the vessels of the aboveground parts of the sporophyte

The accumulation of REEs in the vasculature prompted us to investigate in more detail the REE distribution inside the frond tissue. To do so, we performed elemental μXRF mapping on thin cryosections of pinnules and rachis. The use of cryosections avoids freeze-drying of the samples and preserves tissue and cell integrity, maintaining the actual elemental distribution during the analysis[60]. Due to the specifications of the LUCIA beamline, the incident energy is limited to 8.2 keV, and the Yb distribution could not be analyzed.

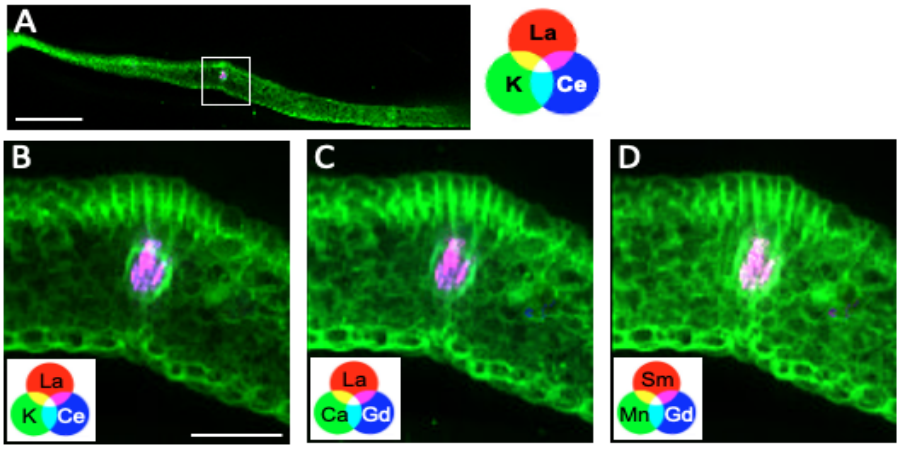

Figure 4. REE distribution inside the vessels of pinnules of *Dryopteris erythrosora*. La-K-Ce (left), La-Ca-Gd (middle) and Sm-Mn-Gd (right) X-ray fluorescence elemental maps were obtained from frozen hydrated cross sections of pinnules of ferns grown on soil supplemented with equal amounts (333 kg^{-1} DW each) of La, Ce, Sm, Gd and Yb. The images were acquired with a step size of 10 µm (A) or 3 µm (B-D), a dwell time of 100 ms (A) or 500 ms (B-D) per pixel, and the energy of the incident beam was set at 7.3 keV. The central vein of (A) is magnified in B-D. The scale bar represents 300 µm (A) or 100 µm (B-D). The color scale is the same for a given element for all the maps.

The XRF maps of frozen-hydrated cross sections of pinnules evidenced the presence of REEs inside the main vein rather than in the surrounding cells of the bundle sheath (Figure 4, Figure

S6), which could not be inferred from Figures 2 and 3. This observation remained valid for all the REEs detected (La, Ce, Sm, Gd) that colocalized inside the veins (Figure 4, Figure S6). Although the specific cell type was not achieved due to the spatial resolution limitation, the central position of the REE signal in the vein is evocative of a xylem distribution[61]. The high-resolution maps in Figure S6 show replicates of pinnule cross sections from high-REE-exposed plants, revealing that although REEs are observed only in the vessels (Figure S6), their distribution is not fully homogeneous, with cross sections from the same exposure conditions showing a variable REE content between cross sections. This result is in accordance with the relatively uneven REE distribution observed in Figure 3.

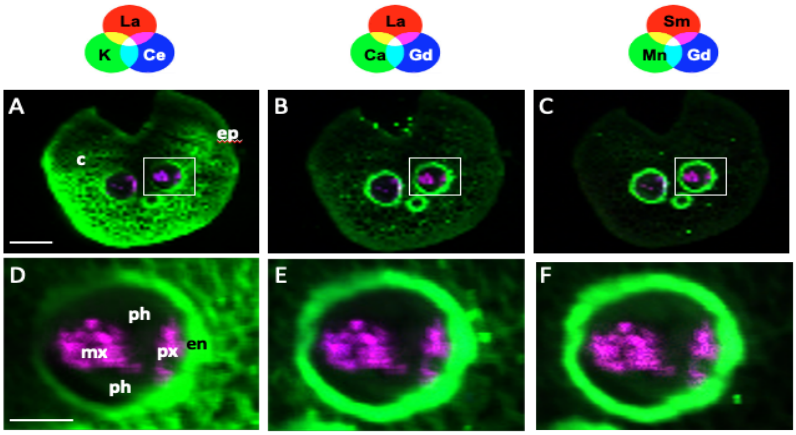

Figure 5. REE distribution inside the rachis of *Dryopteris erythrosora*. La-K-Ce (left panels), La-Ca-Gd (middle panels), and Sm-Mn-Gd (right panels) X-ray fluorescence elemental maps were obtained from frozen hydrated cross sections of rachis of ferns grown on soil supplemented with equal amounts (333 mg kg^{-1} DW each) of La, Ce, Sm, Gd and Yb. The images were acquired with a step size of 20 µm (A-C) or 3 µm (D-F), a dwell time of 100 ms (A-C) or 500 ms (D-F) per pixel, and the energy of the incident beam was set at 7.3 keV. A vascular bundle of (A-C) is magnified in D-F. The scale bar represents 250 µm (A-C) or 50 µm (D-F). The color scale is the same for a given element for all the samples. c: cortex, en: endodermis, ep: epidermis, mx: metaxylem, ph: phloem, px: protoxylem.

In the rachis of the frond, REEs were also found inside the conductive tissues (Figure 5, Figure S7), as shown by the detection of La, Ce, Gd and Sm inside the vascular bundles. The rachis

cross section replicates obtained from different plants showed the same REE distribution in cells inside the veins but not in the cortex or epidermis (Figure 5A-F), thereby strengthening our observations. Furthermore, as confirmed by the carmino-green staining shown in Figure S8 and according to the literature[62], these specific cells were identified as xylem vessels. Even at this scale, REE localization was distinct from the localization of nutrients such as K and Ca (Figure 5, Figure S7), which are present mainly in the endodermis, cortex and epidermis. The apparent superimposition of REEs and Mn patterns in the stele shown in Figure 2 is therefore reassessed by the acquisitions done with cross sections in Figure 5F and Figure S7, since Mn was predominantly detected in the endodermis rather than inside the vascular bundles.

These results clearly illustrate that REEs are transferred to the aerial parts of *D. erythrosora* through the xylem sap and strengthen the hypothesis of REE sequestration inside the vessels. The strategy of accumulating toxic metals in nonphotosynthetic cells is widespread among metal-accumulating plants but more often concerns compartments such as leaf epidermis (e.g., Zn in *Thlaspi caerulescens*[63], Ni and Co in *Glochidion sc. Sericeum*[64]) or trichomes[65,66].

The REE storage inside the vessels could reflect strong molecular interactions between REEs and xylem sap compounds or cell wall components. Only a few studies have investigated REE interactions in plants, with two main findings: (i) In the REE-hyperaccumulating fern *D. linearis*, codeposits of silicon and LREEs were evidenced[67], leading the authors to hypothesize that these mineral complexes could be involved in REE detoxification. However, these deposits were not detected specifically in the vessels, and HREEs were not analyzed in this plant given the absence of HREE contamination; and (ii) in leaf extracts of *D. linearis*[68], a putative LREE-binding molecule, a 2.2-kD peptide has also been identified and evidenced after leaf grinding, a step prone to artifacts. Assuming that this LREE-peptide complex was present in the vessels and

could prevent the transfer of LREEs out of the vessels (which point was not addressed in the article), a significant proportion of LREEs was recovered in the epidermis of *D. linearis*. The very scarce literature on REE interactions in plants does not allow the drawing of clear conclusions regarding REE ligands or sequestration processes. However, the different distribution of REEs between *D. erythrosora* and *D. linearis* supports the hypothesis that the sequestration pattern of REEs in the vessels of *D. erythrosora* is unlikely to follow the same pathway as *D. linearis*. Furthermore, investigations are needed to compare both fern models with respect to chelators present in the xylem sap as well as putative molecular mechanisms of REE unloading and redistribution in adjacent tissues.

Necrotic tissues are not storage sites for REEs but reveal differential mobility of LREEs *vs* HREEs

Several fronds of *D. erythrosora* displayed necrotic tissues in restrained zones. This phenomenon was abundant in the fronds of *D. linearis* exposed to a high REE-contaminated soil[31], which was hypothesized to be a detoxification mechanism. Therefore, we analyzed the REE content and distribution in necrotic areas of *D. erythrosora*. The necrotic tips of either the pinnule or the frond of plants grown in high REE contamination (Figure 2, Figure S4A, Figure 6) presented a noticeable REE signal relative to the limb, which was the least REE-concentrated part of the pinna. The necrotic pinna tip was depleted of K, unlike Mn (Figure 6A) and Ca (Figure S9), reflecting the differential remobilization potential of these nutrients and the similar behavior of REEs in contrasting exposure contexts. As a major component of cell ionic strength, K is more abundant in biologically active cells and is mobile, whereas Ca is less mobile due to its contribution to cell walls[69]. Conversely, Mn follows the transpiration flux but is poorly redistributed through the phloem sap[70]. Therefore, REEs likely reach the pinna tip *via*

370 transpiration-driven xylem flux and are subsequently blocked in the vessels of necrotic tissues,
371 unlike mobile elements such as K.

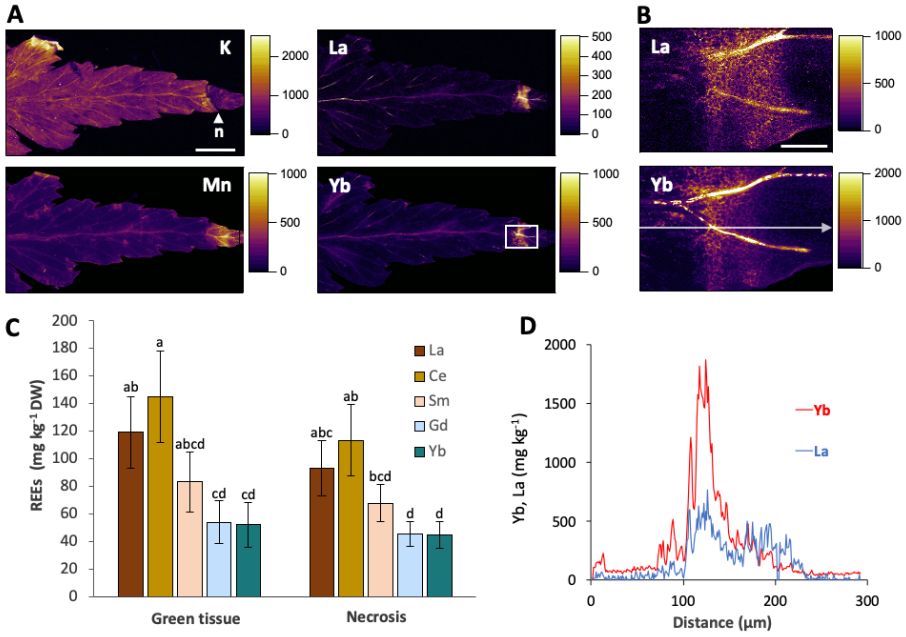

Figure 6. REE distribution and concentrations in the necrotic regions of fronds of *Dryopteris erythrosora*. (A) X-ray fluorescence elemental maps were obtained from frond tips of ferns grown on soil supplemented with equal amounts (333 mg kg^{-1} DW each) of La, Ce, Sm, Gd and Yb. n: necrotic area. (B) is a high-resolution scan of the area selected in (A). The images of this representative sample were acquired with a step size of 20 µm (A) or 5 µm (B) and a dwell time of 20 ms (A) or 5 ms (B) per pixel. The scale bar represents 250 µm (A) or 70 µm (B). (C) REE concentrations in the green and necrotic tissues of the fronds, mean of 3 replicates ± SD. Different letters denote significant differences between REEs ($P < 0.05$, analysis of variance (ANOVA)). (D) REE concentrations along the arrow drawn on the Yb map (B).

372 Despite the more intense REE signal in necrotic parts, REE concentrations measured by ICP-MS
373 in healthy and necrotic tissues of the pinna were similar (Figure 6C), suggesting that necrotic
374 tissues are not the main accumulation sites for REEs in this species, at least for this range of REE
375 concentrations, unlike the observations for the REE-accumulating fern *Dicranopteris linearis*[31]
376 or other elements such as As in the As-accumulating fern *Pteris vittata*[71].

The REE diffusion outside the veins observed in the necrosis (Figure 2 and Figure 6A, B) could be due to the loss of vascular tissue integrity leading to sap leakage, which would indicate that although REEs could be locked up within the vessels, a significant proportion would remain mobile in xylem vessels. La and Yb distributions were further analyzed through an elemental profile in the necrotic area (cf. white arrow in Figure 6B, profile in Figure 6D). Along this profile a living area (rich in K), a vein and a necrotic zone, the REEs did not show an identical distribution. On the one hand, the living area (left side of the vein) had a low REE relative content, which increased in the vein for both La and Yb. This observation is consistent with the vascular distribution of the REEs previously described. On the other hand, in the necrotic part, on the right of the vein, the La content was of the same order of magnitude as the order of magnitude found in the vein, whereas the Yb concentration decreased strongly. Such a different behavior between these contrasted REEs (La as an LREE and Yb as an HREE) could depict a higher mobility of La or a stronger binding of Yb in this necrosis.

REEs are not stored in the root vessels of the sporophyte but are immobilized in the rhizoids of the gametophyte

MicroXRF mapping performed on thin cryosections of *D. erythrosora* roots showed an REE tissue distribution in contrast to the tissue distribution of the aboveground parts. Indeed, in Figure S10, the REEs are present in the root rhizodermis and in cell layers surrounding the central cylinder instead of sap-conducting cells. The rhizodermal relative REE enrichment likely reflects apoplastic REE uptake from the growing substrate. REEs were detected in the cortex cells surrounding the endodermis and the endodermis itself, while the central cylinder apparently contains fewer REEs. In contrast to the fronds, REEs were not stored in the root veins but rather detected in the central cylinder only in one single root cross section (Figure S10). The same trend

400 was observed for young and old roots, as shown in Figure S10. Further investigations would be
401 advisable, notably cross sections obtained at different distances from the root tip, to better
402 describe and understand the REE loading into the vessels. However, transfer into the xylem of
403 aboveground parts seems to be a deadlock for REEs unless vessel integrity is impaired, as
404 illustrated by the necrosis REE leakage described above. It could possibly be due to a transporter
405 with a root-specific expression pattern, which therefore would only allow REE loading into the
406 xylem, whereas no export system would permit REE unloading from the xylem to the
407 surrounding parenchyma cells of the fronds. A second hypothesis would involve a change in
408 REE speciation during sap transport (e.g. REE precipitation or binding), that would no longer
409 allow REEs to be unloaded from the veins. Therefore, further studies aiming at elucidating the
410 solubility of REEs and at identifying REE ligands in the xylem sap or on vessel cell walls are
411 crucial to unravel this vascular storage of REEs.

412 REE accumulation sites have also been investigated by μXRF in the gametophyte stage of the
413 fern grown *in vitro* and exposed to a mix of the five REEs. The gametophyte corresponds to the
414 haploid developmental stage of the *D. erythrosora* lifecycle and consists of a photosynthetic
415 blade with thin single-cell rhizoids involved in anchoring as well as water and nutrient
416 absorption[72] (Figure S11A). Only the rhizoids contained REEs, and colocalization of the
417 different REEs was observed (Figure S11). The K content of the photosynthetic tissue proves the
418 biologically active state of these cells, and once more, the Ca and Mn distributions differed from
419 the distributions of La and Gd (Figure S11). Due to insufficient spatial resolution, it was not
420 possible to decipher whether the REEs accumulated in the intracellular or apoplastic
421 compartment of the rhizoids; however, no REE transfer to the photosynthetic part was detected,
422 suggesting that REEs are transferred to photosynthetic organs solely in the vascularized

sporophyte following xylem flux and that no cell-to-cell mobility is allowed for REEs in the vein-lacking gametophyte.

Altogether, the results of the present study and the literature showed that, even if REE accumulation is a conserved trait among ferns[25,30], REE distribution has common features but also peculiarities across fern phylogeny. The main characteristic of *D. erythrosora* is the storage of REEs in xylem vessels only (not encountered in *D. linearis*), which could be the result of REE accumulation mechanisms having evolved differently between these fern genera (different transport systems and/or various REE ligands produced by the plants). Further comparative genomic, transcriptomic and metabolic analyses between these REE accumulating ferns are the next step towards identifying the mechanisms underlying the specificities of accumulation we highlighted. To conclude, our results set a new basis for a better understanding of REE transfer and accumulation in plants, which is still in its infancy.

AVAILABILITY OF DATA AND MATERIEL

The authors declare that all data related to the findings of this study are available within the article and supplementary information or are available from the corresponding author upon reasonable request.

ACKNOWLEDGMENTS

We acknowledge the financial support from the French National Research Agency through the national program 'Investissements d'avenir' with the reference ANR-10-LABX-21-01/LABEX RESSOURCES21, the French National programs EC2CO-ECODYN (RAREFERN), CNRS-MITI Métallo-mix (LIGREE-219112), the Inter-Carnot ICEEL (REECOVERY) and from the Région Grand Est. We acknowledge DESY (Hamburg, Germany), a member of the Helmholtz

Association HGF, for the provision of experimental facilities. Parts of this research were carried out at P06. Beamtime was allocated as part of the inhouse research program (KMS). The research leading to this result has been supported by the project CALIPSOplus under Grant Agreement 730872 from the EU Framework Programme for Research and Innovation HORIZON 2020. Part of this work was performed at the LUCIA beamline at Synchrotron SOLEIL (project 20180105). This work is included in the scientific program of the GISFI research consortium (Groupement d'Intérêt Scientifique sur les Friches Industrielles). We acknowledge Dr Nadia Morin-Crini of the PEAT² platform for the ICP-MS analyses, Christine Friry for technical support with plant growth, and Dr Gerald Falkenberg for helpful discussions.

FUNDING SOURCES

This work was supported by the French National Research Agency through the national program 'Investissements d'avenir' with the reference ANR-10-LABX-21-01/LABEX RESSOURCES21, the French National programs EC2CO-ECODYN (RAREFERN), CNRS-MITI Metallo-mix (LIGREE-219112), the Inter-Carnot ICEEL (REECOVERY) and by the Région Grand Est. The research leading to this result has been supported by the project CALIPSOplus under Grant Agreement 730872 from the EU Framework Programme for Research and Innovation HORIZON 2020.

AUTHOR INFORMATION

Corresponding Author

Dr Marie Le Jean

Tel: +33-3-72-74-89-95

E-mail: marie.lejean@univ-lorraine.fr

Present Addresses

† *Biology Department, Brookhaven National Laboratory, Upton, NY 11973, USA*

Author Contributions

MLJ: Investigation, Conceptualization, Formal analysis, Project funding, Writing – review & editing. EMP: Conceptualization, Formal analysis, Writing – review & editing. CR: Investigation, Formal analysis, Writing – review & editing. NG: Investigation, Formal analysis, Writing – review & editing. MC: Investigation, Writing – review & editing. DV: Investigation, Writing – review & editing. KS: Investigation, Formal analysis, Writing – review & editing. DB: Investigation, Conceptualization, Formal analysis, Project funding, Writing – review & editing. All authors have given approval to the final version of the manuscript.

REFERENCES

(1) Connelly, N. G.; Royal Society of Chemistry (Great Britain); International Union of Pure and Applied Chemistry. *Nomenclature of Inorganic Chemistry*; Royal Society of Chemistry, 2005.

(2) Beaudry, B. J.; Gschneidner, K. A. Chapter 2 Preparation and Basic Properties of the Rare Earth Metals. *Handb. Phys. Chem. Rare Earths* **1978**, *1*, 173–232. https://doi.org/10.1016/S0168-1273(78)01006-5.

(3) Zhou, B.; Li, Z.; Chen, C. Global Potential of Rare Earth Resources and Rare Earth Demand from Clean Technologies. *Minerals* **2017**, *7* (203), 1–14.

https://doi.org/10.3390/min7110203.

(4) Copetti, D.; Finsterle, K.; Marziali, L.; Stefani, F.; Tartari, G.; Douglas, G.; Reitzel, K.; Spears, B. M.; Winfield, I. J.; Crosa, G.; D'Haese, P.; Yasseri, S.; Lürling, M. Eutrophication Management in Surface Waters Using Lanthanum Modified Bentonite: A Review. *Water Res.* **2016**, *97*, 162–174. https://doi.org/10.1016/j.watres.2015.11.056.

(5) Han, Y.; Zhang, Y.; Li, Q.; Lürling, M.; Li, W.; He, H.; Gu, J.; Li, K.; Kuanyi Li, C.; Key, S. Submerged Macrophytes Benefit from Lanthanum Modified Bentonite Treatment under Juvenile Omni-Benthivorous Fish Disturbance: Implications for Shallow Lake Restoration. *Freshw. Biol.* **2022**, *67* (4), 672–683. https://doi.org/10.1111/FWB.13871.

(6) Pang, X.; Li, D.; Peng, A. Application of Rare-Earth Elements in the Agriculture of China and Its Environmental Behavior in Soil. *Environ. Sci. Pollut. Res.* **2002**, *9* (2), 143.

(7) Ciacci, L.; Reck, B. K.; Nassar, N. T.; Graedel, T. E. Lost by Design. *Environ. Sci. Technol.* **2015**, *49* (16), 9443–9451. https://doi.org/10.1021/es505515z.

(8) Hatje, V.; Bruland, K. W.; Flegal, A. R. Increases in Anthropogenic Gadolinium Anomalies and Rare Earth Element Concentrations in San Francisco Bay over a 20 Year Record. *Environ. Sci. Technol.* **2016**, *50* (8), 4159–4168. https://doi.org/10.1021/acs.est.5b04322.

(9) Hissler, C.; Stille, P.; Guignard, C.; Iffly, J. F.; Pfister, L. Rare Earth Elements as Hydrological Tracers of Anthropogenic and Critical Zone Contributions: A Case Study at the Alzette River Basin Scale. *Procedia Earth Planet. Sci.* **2014**, *10*, 349–352. https://doi.org/10.1016/j.proeps.2014.08.036.

(10) Ramos, S. J.; Dinali, G. S.; Oliveira, C.; Martins, G. C.; Moreira, C. G.; Siqueira, J. O.; Guilherme, L. R. G. Rare Earth Elements in the Soil Environment. *Curr. Pollut. Reports*

2016. https://doi.org/10.1007/s40726-016-0026-4.

(11) Tyler, G. Rare Earth Elements in Soil and Plant Systems - A Review. *Plant Soil* **2004**, *267* (1–2), 191–206. https://doi.org/10.1007/s11104-005-4888-2.

(12) Xiangsheng, L.; Jiachen, W.; Jun, Y.; Yubin, F.; Yanping, W.; He, Z. Application of Rare Earth Phosphate Fertilizer in Western Area of China. *J. Rare Earths* **2006**, *24* (1), 423–426. https://doi.org/10.1016/S1002-0721(07)60418-9.

(13) Ribeiro, P. G.; Dinali, G. S.; Boldrin, P. F.; de Carvalho, T. S.; de Oliveira, C.; Ramos, S. J.; Siqueira, J. O.; Moreira, C. G.; Guilherme, L. R. G. Rare Earth Elements (REEs) Rich-Phosphate Fertilizers Used in Brazil Are More Effective in Increasing Legume Crops Yield Than Their REEs-Poor Counterparts. *Int. J. Plant Prod. 2021 151* **2021**, *15* (1), 1–11. https://doi.org/10.1007/S42106-021-00129-5.

(14) Agathokleous, E.; Kitao, M.; Calabrese, E. J. The Rare Earth Element (REE) Lanthanum (La) Induces Hormesis in Plants. *Environ. Pollut.* **2018**, *238*, 1044–1047. https://doi.org/10.1016/j.envpol.2018.02.068.

(15) Técher, D.; Grosjean, N.; Sohm, B.; Blaudez, D.; Le Jean, M. Not Merely Noxious? Time-Dependent Hormesis and Differential Toxic Effects Systematically Induced by Rare Earth Elements in Escherichia Coli. *Environ. Sci. Pollut. Res. 2019 275* **2020**, *27* (5), 5640–5649. https://doi.org/10.1007/S11356-019-07002-Z.

(16) Hu, Z.; Richter, H.; Sparovek, G.; Schnug, E. Physiological and Biochemical Effects of Rare Earth Elements on Plants and Their Agricultural Significance: A Review. *J. Plant Nutr.* **2004**, *27* (1), 183–220. https://doi.org/10.1081/PLN-120027555.

(17) Agathokleous, E.; Zhou, B.; Geng, C.; Xu, J.; Saitanis, C. J.; Feng, Z.; Tack, F. M. G.; Rinklebe, J. Mechanisms of Cerium-Induced Stress in Plants: A Meta-Analysis. *Sci. Total*

Environ. **2022**, *852*, 158352. https://doi.org/10.1016/J.SCITOTENV.2022.158352.

(18) Malhotra, N.; Hsu, H. S.; Liang, S. T.; Roldan, M. J. M.; Lee, J. S.; Ger, T. R.; Hsiao, C. Der. An Updated Review of Toxicity Effect of the Rare Earth Elements (REEs) on Aquatic Organisms. *Anim. 2020, Vol. 10, Page 1663* **2020**, *10* (9), 1663. https://doi.org/10.3390/ANI10091663.

(19) Blinova, I.; Muna, M.; Heinlaan, M.; Lukjanova, A.; Kahru, A. Potential Hazard of Lanthanides and Lanthanide-Based Nanoparticles to Aquatic Ecosystems: Data Gaps, Challenges and Future Research Needs Derived from Bibliometric Analysis. *Nanomaterials* **2020**, *10* (2), 328. https://doi.org/10.3390/nano10020328.

(20) Grosjean, N.; Le Jean, M.; Chalot, M.; Mora-Montes, H. M.; Armengaud, J.; Gross, E. M.; Blaudez, D. Genome-Wide Mutant Screening in Yeast Reveals That the Cell Wall Is a First Shield to Discriminate Light From Heavy Lanthanides. *Front. Microbiol.* **2022**, *13*. https://doi.org/10.3389/FMICB.2022.881535.

(21) Grosjean, N.; Le Jean, M.; Armengaud, J.; Schikora, A.; Chalot, M.; Gross, E. M.; Blaudez, D. Combined Omics Approaches Reveal Distinct Responses between Light and Heavy Rare Earth Elements in Saccharomyces Cerevisiae. *J. Hazard. Mater.* **2022**, *425*, 127830. https://doi.org/10.1016/J.JHAZMAT.2021.127830.

(22) Pallares, R. M.; Faulkner, D.; An, D. D.; Hébert, S.; Loguinov, A.; Proctor, M.; Villalobos, J. A.; Bjornstad, K. A.; Rosen, C. J.; Vulpe, C.; Abergel, R. J. Genome-Wide Toxicogenomic Study of the Lanthanides Sheds Light on the Selective Toxicity Mechanisms Associated with Critical Materials. *Proc. Natl. Acad. Sci. U. S. A.* **2021**, *118* (18). https://doi.org/10.1073/PNAS.2025952118.

(23) Burges, A.; Alkorta, I.; Epelde, L.; Garbisu, C. From Phytoremediation of Soil

Contaminants to Phytomanagement of Ecosystem Services in Metal Contaminated Sites. *Int. J. Phytoremediation* **2018**, *20* (4), 384–397. https://doi.org/https://doi.org/10.1080/15226514.2017.1365340.

(24) Van der Ent, A.; Echevarria, G.; Baker, A. J. M.; Morel, J. L. Agromining: Farming for Metals. *Agromining Farming Met. Springer Cham, Switz.* **2018**, 75–92.

(25) Ozaki, T.; Enomoto, S.; Minai, Y.; Ambe, S.; Ambe, F.; Tominaga, T. Determination of Lanthanides and Other Trace Elements in Ferns by Instrumental Neutron Activation Analysis. *J. Radioanal. Nucl. Chem.* **1997**, *217* (1), 117–124. https://doi.org/10.1007/BF02055359.

(26) Ozaki, T.; Enomoto, S.; Minai, Y.; Ambe, S.; Makide, Y. A Survey of Trace Elements in Pteridophytes. *Biol. Trace Elem. Res.* **2000**, *74* (3), 259–273. https://doi.org/10.1385/bter:74:3:259.

(27) Ichihashi, H.; Morita, H.; Tatsukawa, R. Rare Earth Elements (REEs) in Naturally Grown Plants in Relation to Their Variation in Soils. *Environ. Pollut.* **1992**, *76* (2), 157–162. https://doi.org/10.1016/0269-7491(92)90103-H.

(28) Yuan, M.; Liu, C.; Liu, W.-S.; Guo, M.-N.; Morel, J. L.; Huot, H.; Yu, H.-J.; Tang, Y.-T.; Qiu, R.-L. Accumulation and Fractionation of Rare Earth Elements (REEs) in the Naturally Grown *Phytolacca Americana* L. in Southern China. *Int. J. Phytoremediation* **2018**, *20* (5), 415–423. https://doi.org/10.1080/15226514.2017.1365336.

(29) Wood, B. W.; Grauke, L. J. The Rare-Earth Metallome of Pecan and Other Carya. *J. Am. Soc. Hortic. Sci.* **2011**, *136* (6), 389–398. https://doi.org/10.21273/JASHS.136.6.389.

(30) Grosjean, N.; Blaudez, D.; Chalot, M.; Gross, E. M.; Le Jean, M. Identification of New Hardy Ferns That Preferentially Accumulate Light Rare Earth Elements: A Conserved

583 Trait within Fern Species. *Environ. Chem.* **2020**, *17* (2), 191–200.
584 https://doi.org/10.1071/EN19182.
585 (31) Liu, W. S.; Van Der Ent, A.; Erskine, P. D.; Morel, J. L.; Echevarria, G.; Spiers, K. M.;
586 Montargès-Pelletier, E.; Qiu, R. L.; Tang, Y. T. Spatially Resolved Localization of
587 Lanthanum and Cerium in the Rare Earth Element Hyperaccumulator Fern Dicranopteris
588 Linearis from China. *Environ. Sci. Technol.* **2020**, *54* (4), 2287–2294.
589 https://doi.org/10.1021/acs.est.9b05728.
590 (32) Grosjean, N.; Le Jean, M.; Berthelot, C.; Chalot, M.; Gross, E. M.; Blaudez, D.
591 Accumulation and Fractionation of Rare Earth Elements Are Conserved Traits in the
592 Phytolacca Genus. *Sci. Rep.* **2019**, *9* (1). https://doi.org/10.1038/s41598-019-54238-3.
593 (33) Wang, X. P.; Shan, X. Q.; Zhang, S. Z.; Wen, B. Distribution of Rare Earth Elements
594 among Chloroplast Components of Hyperaccumulator Dicranopteris Dichotoma. *Anal.*
595 *Bioanal. Chem.* **2003**, *376* (6), 913–917. https://doi.org/10.1007/S00216-003-2014-
596 Y/FIGURES/2.
597 (34) Wei, Z.; Hong, F.; Yin, M.; Li, H.; Hu, F.; Zhao, G.; Woonchungwong, J. Subcellular and
598 Molecular Localization of Rare Earth Elements and Structural Characterization of Yttrium
599 Bound Chlorophyll a in Naturally Grown Fern Dicranopteris Dichotoma. *Microchem. J.*
600 **2005**. https://doi.org/10.1016/j.microc.2004.07.005.
601 (35) Lai, Y.; Wang, Q.; Yang, L.; Huang, B. Subcellular Distribution of Rare Earth Elements
602 and Characterization of Their Binding Species in a Newly Discovered Hyperaccumulator
603 Pronephrium Simplex. *Talanta* **2006**, *70* (1), 26–31.
604 https://doi.org/10.1016/j.talanta.2005.12.062.
605 (36) Chen, Z.; Chen, Z. Effects of Ecological Restoration Measures on the Distribution of

606 Dicranopteris Dichotoma at the Microscale in the Red Soil Hilly Region of China. *PLoS*
607 *One* **2018**, *13* (10), e0204743. https://doi.org/10.1371/JOURNAL.PONE.0204743.
608 (37) Ozaki, T.; Enomoto, S.; Minai, Y.; Ambe, S.; Ambe, F.; Tominaga, T. Determination of
609 Lanthanides and Other Trace Elements in Ferns by Instrumental Neutron Activation
610 Analysis. *J. Radioanal. Nucl. Chem.* **1997**, *217* (1), 117–124.
611 https://doi.org/10.1007/BF02055359.
612 (38) Castillo-Michel, H. A.; Larue, C.; Pradas del Real, A. E.; Cotte, M.; Sarret, G. Practical
613 Review on the Use of Synchrotron Based Micro- and Nano- X-Ray Fluorescence Mapping
614 and X-Ray Absorption Spectroscopy to Investigate the Interactions between Plants and
615 Engineered Nanomaterials. *Plant Physiol. Biochem.* **2017**, *110*, 13–32.
616 https://doi.org/10.1016/J.PLAPHY.2016.07.018.
617 (39) Schroer, C. G.; Boye, P.; Feldkamp, J. M.; Patommel, J.; Samberg, D.; Schropp, A.;
618 Schwab, A.; Stephan, S.; Falkenberg, G.; Wellenreuther, G.; Reimers, N. Hard X-Ray
619 Nanoprobe at Beamline P06 at PETRA III. *Nucl. Instruments Methods Phys. Res. Sect. A*
620 *Accel. Spectrometers, Detect. Assoc. Equip.* **2010**, *616* (2–3), 93–97.
621 https://doi.org/10.1016/J.NIMA.2009.10.094.
622 (40) Boesenberg, U.; Ryan, C. G.; Kirkham, R.; Siddons, D. P.; Alfeld, M.; Garrevoet, J.;
623 Núñez, T.; Claussen, T.; Kracht, T.; Falkenberg, G. Fast X-Ray Microfluorescence
624 Imaging with Submicrometer-Resolution Integrating a Maia Detector at Beamline P06 at
625 PETRA III. *J. Synchrotron Radiat.* **2016**, *23* (Pt 6), 1550–1560.
626 https://doi.org/10.1107/S1600577516015289.
627 (41) Siddons, D. P.; Kirkham, R.; Ryan, C. G.; De Geronimo, G.; Dragone, A.; Kuczewski, A.
628 J.; Li, Z. Y.; Carini, G. A.; Pinelli, D.; Beuttenmuller, R.; Elliott, D.; Pfeffer, M.; Tyson,

T. A.; Moorhead, G. F.; Dunn, P. A. Maia X-Ray Microprobe Detector Array System. *J. Phys. Conf. Ser.* **2014**, *499* (1), 012001. https://doi.org/10.1088/1742-6596/499/1/012001.

(42) Ryan, C. G.; Siddons, D. P.; Kirkham, R.; Li, Z. Y.; De Jonge, M. D.; Paterson, D. J.; Kuczewski, A.; Howard, D. L.; Dunn, P. A.; Falkenberg, G.; Boesenberg, U.; De Geronimo, G.; Fisher, L. A.; Halfpenny, A.; Lintern, M. J.; Lombi, E.; Dyl, K. A.; Jensen, M.; Moorhead, G. F.; Cleverley, J. S.; Hough, R. M.; Godel, B.; Barnes, S. J.; James, S. A.; Spiers, K. M.; Alfeld, M.; Wellenreuther, G.; Vukmanovic, Z.; Borg, S. Maia X-Ray Fluorescence Imaging: Capturing Detail in Complex Natural Samples. *J. Phys. Conf. Ser.* **2014**, *499* (1), 1–12. https://doi.org/10.1088/1742-6596/499/1/012002.

(43) Kopittke, P. M.; Punshon, T.; Paterson, D. J.; Tappero, R. V.; Wang, P.; Pax, F.; van der Ent, A.; Lombi, E. Synchrotron-Based X-Ray Fluorescence Microscopy as a Technique for Imaging of Elements in Plants. *Plant Physiol.* **2018**, *178* (2), 507–523. https://doi.org/10.1104/PP.18.00759.

(44) van der Ent, A.; Przybyłowicz, W. J.; de Jonge, M. D.; Harris, H. H.; Ryan, C. G.; Tylko, G.; Paterson, D. J.; Barnabas, A. D.; Kopittke, P. M.; Mesjasz-Przybyłowicz, J. X-Ray Elemental Mapping Techniques for Elucidating the Ecophysiology of Hyperaccumulator Plants. *New Phytol.* **2018**, *218* (2), 432–452. https://doi.org/10.1111/NPH.14810.

(45) Flank, A. M.; Cauchon, G.; Lagarde, P.; Bac, S.; Janousch, M.; Wetter, R.; Dubuisson, J. M.; Idir, M.; Langlois, F.; Moreno, T.; Vantelon, D. LUCIA, a Microfocus Soft XAS Beamline. *Nucl. Instruments Methods Phys. Res. Sect. B Beam Interact. with Mater. Atoms* **2006**, *246* (1), 269–274. https://doi.org/10.1016/J.NIMB.2005.12.007.

(46) Vantelon, D.; Trcera, N.; Roy, D.; Moreno, T.; Mailly, D.; Guilet, S.; Metchalkov, E.; Delmotte, F.; Lassalle, B.; Lagarde, P.; Flank, A. M. The LUCIA Beamline at SOLEIL. *J.*

652 *Synchrotron Radiat.* **2016**, *23* (2), 635–640. https://doi.org/10.1107/S1600577516000746.
653 (47) Ryan, C. G.; Jamieson, D. N. Dynamic Analysis: On-Line Quantitative PIXE
654 Microanalysis and Its Use in Overlap-Resolved Elemental Mapping. *Nucl. Instruments*
655 *Methods Phys. Res. Sect. B Beam Interact. with Mater. Atoms* **1993**, *77* (1–4), 203–214.
656 https://doi.org/10.1016/0168-583X(93)95545-G.
657 (48) Ryan, C. G. Quantitative Trace Element Imaging Using PIXE and the Nuclear
658 Microprobe. *Int. J. Imaging Syst. Technol.* **2000**, *11* (4), 219–230.
659 https://doi.org/10.1002/IMA.1007.
660 (49) Ryan, C. G.; Cousens, D. R.; Sie, S. H.; Griffin, W. L. Quantitative Analysis of PIXE
661 Spectra in Geoscience Applications. *Nucl. Instruments Methods Phys. Res. Sect. B Beam*
662 *Interact. with Mater. Atoms* **1990**, *49* (1–4), 271–276. https://doi.org/10.1016/0168-
663 583X(90)90259-W.
664 (50) Ryan, C. G.; Etschmann, B. E.; Vogt, S.; Maser, J.; Harland, C. L.; Van Achterbergh, E.;
665 Legnini, D. Nuclear Microprobe – Synchrotron Synergy: Towards Integrated Quantitative
666 Real-Time Elemental Imaging Using PIXE and SXRF. *Nucl. Instruments Methods Phys.*
667 *Res. Sect. B Beam Interact. with Mater. Atoms* **2005**, *231* (1–4), 183–188.
668 https://doi.org/10.1016/J.NIMB.2005.01.054.
669 (51) Solé, V. A.; Papillon, E.; Cotte, M.; Walter, P.; Susini, J. A Multiplatform Code for the
670 Analysis of Energy-Dispersive X-Ray Fluorescence Spectra. *Spectrochim. Acta Part B At.*
671 *Spectrosc.* **2007**, *62* (1), 63–68. https://doi.org/10.1016/J.SAB.2006.12.002.
672 (52) Schindelin, J.; Arganda-Carreras, I.; Frise, E.; Kaynig, V.; Longair, M.; Pietzsch, T.;
673 Preibisch, S.; Rueden, C.; Saalfeld, S.; Schmid, B.; Tinevez, J. Y.; White, D. J.;
674 Hartenstein, V.; Eliceiri, K.; Tomancak, P.; Cardona, A. Fiji: An Open-Source Platform

675 for Biological-Image Analysis. *Nat. Methods 2012 97* **2012**, *9* (7), 676–682.
676 https://doi.org/10.1038/NMETH.2019.
677 (53) Ene, C. D.; Ruta, L. L.; Nicolau, I.; Popa, C. V.; Iordache, V.; Neagoe, A. D.; Farcasanu,
678 I. C. Interaction between Lanthanide Ions and Saccharomyces Cerevisiae Cells. *J. Biol.*
679 *Inorg. Chem.* **2015**, *20* (7), 1097–1107. https://doi.org/10.1007/s00775-015-1291-1.
680 (54) Lim, S.; Franklin, S. J. Lanthanide-Binding Peptides and the Enzymes That Might Have
681 Been. *Cell. Mol. Life Sci.* **2004**, *61* (17), 2184–2188. https://doi.org/10.1007/s00018-004-
682 4156-2.
683 (55) Ozaki, T.; Enomoto, S.; Minai, Y.; Ambe, S.; Makide, Y. A Survey of Trace Elements in
684 Pteridophytes. *Biol. Trace Elem. Res.* **2000**, *74* (3), 259–273.
685 https://doi.org/10.1385/BTER:74:3:259.
686 (56) Djingova, R.; Ivanova, J.; Wagner, G.; Korhammer, S.; Markert, B. Distribution of
687 Lanthanoids, Be, Bi, Ga, Te, TI, Th and U on the Territory of Bulgaria Using Populus
688 Nigra “Italica” as an Indicator. *Sci. Total Environ.* **2001**, *280* (1–3), 85–91.
689 https://doi.org/10.1016/S0048-9697(01)00817-8.
690 (57) Kumar, A.; Pandey, A. K.; Singh, S. S.; Shanker, R.; Dhawan, A. Engineered ZnO and
691 TiO2 Nanoparticles Induce Oxidative Stress and DNA Damage Leading to Reduced
692 Viability of Escherichia Coli. *Free Radic. Biol. Med.* **2011**, *51* (10), 1872–1881.
693 https://doi.org/10.1016/j.freeradbiomed.2011.08.025.
694 (58) Li, J. T.; Gurajala, H. K.; Wu, L. H.; Van Der Ent, A.; Qiu, R. L.; Baker, A. J. M.; Tang,
695 Y. T.; Yang, X. E.; Shu, W. S. Hyperaccumulator Plants from China: A Synthesis of the
696 Current State of Knowledge. *Environ. Sci. Technol.* **2018**, *52* (21), 11980–11994.
697 https://doi.org/10.1021/ACS.EST.8B01060/SUPPL_FILE/ES8B01060_SI_001.PDF.

(59) Küpper, H.; Lombi, E.; Zhao, F. J.; McGrath, S. P. Cellular Compartmentation of Cadmium and Zinc in Relation to Other Elements in the Hyperaccumulator Arabidopsis Halleri. *Planta* **2000**, *212* (1), 75–84. https://doi.org/10.1007/s004250000366.

(60) Matsuyama, S.; Shimura, M.; … M. F.-X.; 2010, undefined. Elemental Mapping of Frozen-hydrated Cells with Cryo-scanning X-ray Fluorescence Microscopy. *Wiley Online Libr.* **2010**, *39* (4), 260–266. https://doi.org/10.1002/xrs.1256.

(61) Doležal, J.; Dvorský, M.; Börner, A.; Wild, J.; Schweingruber, F. H. Anatomical Descriptions of Horsetails and Ferns. *Anatomy, Age Ecol. High Mt. Plants Ladakh, West. Himalaya* **2018**, 35–46. https://doi.org/10.1007/978-3-319-78699-5_2.

(62) Hernandez-Hernandez, V.; Terrazas, T.; Mehltreter, K.; Angeles, G. Studies of Petiolar Anatomy in Ferns: Structural Diversity and Systematic Significance of the Circumendodermal Band. *Bot. J. Linn. Soc.* **2012**, *169* (4), 596–610.

(63) Küpper, H.; Jie Zhao, F.; McGrath, S. Cellular Compartmentation of Zinc in Leaves of the Hyperaccumulator Thlaspi Caerulescens. *Plant Physiol.* **1999**, *119* (1), 305–312. https://doi.org/10.1104/pp.119.1.305.

(64) van der Ent, A.; Mak, R.; de Jonge, M. D.; Harris, H. H. Simultaneous Hyperaccumulation of Nickel and Cobalt in the Tree Glochidion Cf. Sericeum (Phyllanthaceae): Elemental Distribution and Chemical Speciation. *Sci. Rep.* **2018**, *8* (1), 1–15.

(65) Krämer, U.; Grime, G. W.; Smith, J. A. C.; Hawes, C. R.; Baker, A. J. M. Micro-PIXE as a Technique for Studying Nickel Localization in Leaves of the Hyperaccumulator Plant Alyssum Lesbiacum. *Nucl. Instruments Methods Phys. Res. Sect. B Beam Interact. with Mater. Atoms* **1997**, *130* (1–4), 346–350.

(66) Broadhurst, C. L.; Chaney, R. L.; Angle, J. S.; Maugel, T. K.; Erbe, E. F.; Murphy, C. A.

Simultaneous Hyperaccumulation of Nickel, Manganese, and Calcium in Alyssum Leaf Trichomes. *Environ. Sci. Technol.* **2004**, *38* (21), 5797–5802. https://doi.org/10.1021/ES0493796/ASSET/IMAGES/LARGE/ES0493796F00005.JPEG.

(67) Liu, W. S.; Zheng, H. X.; Guo, M. N.; Liu, C.; Huot, H.; Morel, J. L.; van der Ent, A.; Tang, Y. T.; Qiu, R. L. Co-Deposition of Silicon with Rare Earth Elements (REEs) and Aluminium in the Fern Dicranopteris Linearis from China. *Plant Soil* **2019**, *437* (1–2), 427–437. https://doi.org/10.1007/s11104-019-04005-0.

(68) Wang, H.; Shan, X. Q.; Zhang, S.; Wen, B. Preliminary Characterization of a Light-Rare-Earth-Element-Binding Peptide of a Natural Perennial Fern Dicranopteris Dichotoma. *Anal. Bioanal. Chem.* **2003**, *376* (1), 49–52. https://doi.org/10.1007/S00216-003-1853-X/FIGURES/4.

(69) Lincoln, T.; Eduardo, Z. *Plant Physiology*, 4th ed.; Sinuaer associates, Ed.; Sunderland, Massachusetts, 2006.

(70) Andresen, E.; Peiter, E.; Küpper, H. Trace Metal Metabolism in Plants. *J. Exp. Bot.* **2018**, *69* (5), 909–954. https://doi.org/10.1093/jxb/erx465.

(71) Lombi, E.; Zhao, F. J.; Fuhrmann, M.; Ma, L. Q.; McGrath, S. P. Arsenic Distribution and Speciation in the Fronds of the Hyperaccumulator Pteris Vittata. *New Phytol.* **2002**, *156* (2), 195–203. https://doi.org/10.1046/J.1469-8137.2002.00512.X.

(72) Jang, B. K.; Cho, J. S.; Kwon, H. J.; Lee, C. H. Optimal Conditions for Spore Germination and Gametophyte and Sporophyte Production in the Autumn Fern Dryopteris Erythrosora. *Hortic. Environ. Biotechnol.* **2019**, *60* (1), 115–123. https://doi.org/10.1007/s13580-018-0097-9.

Supplemental text (Material and Methods)

Cultivation of ferns hydroponically

For the cultivation of ferns in hydroponics, roots of plants precultivated on loam were first carefully washed before transfer to the hydroponic solution made of a modified quarter-strength Hoagland medium (2 mM NH_4NO_3, 3 mM KNO_3, 2 mM KCl, 2 mM $Ca(NO_3)_2 \cdot 4H_2O$, 2 mM $MgSO_4 \cdot 7H2O$, 1.5 mM NaCl, 600 µM KH_2PO_4, 100 µM $CaCl_2$, 50 µM NaFe(III)-EDTA, 50 µM H_3BO_3, 5 µM $MnCl_2 \cdot 4H_2O$, 10 µM $ZnSO_4 \cdot 7H_2O$, 0.5 µM $CuSO_4 \cdot 5H_2O$, 0.1 µM Na_2MoO_3, pH 5.6) under constant aeration. Ferns were grown for four weeks in the control nutritive medium and subsequently transferred for three weeks to the same solution containing 10 μM of both La and Yb and lacking KH_2PO_4 to avoid REE precipitation with phosphates. After three weeks of exposure to REEs, plants were harvested, and a subset of plants was reintroduced to the noncontaminated solution for two extra weeks and further harvested and analyzed identically.

Cultivation of gametophytes *in vitro*

Gametophyte cultures were performed from spores of *D. erythrosora*. Spores were surface sterilized first with 70% ethanol for one min and then with 10% bleach for 20 min, rinsed three times in sterile water and sown on agar plates containing half-strength MS medium without phosphate to avoid REEs precipitation (10.3 mM NH_4NO_3, 9.4 mM KNO_3, 1.5 mM $CaCl_2$, 0.625 mM, 0.75 mM $MgSO_4 \cdot 7H2O$, 50 µM NaFe(III)-EDTA, 50 µM H_3BO_3, 50 µM $MnCl_2 \cdot 4H_2O$, 15 µM $ZnSO_4 \cdot 7H_2O$, 2.5 µM KI, 0.5 µM $CuSO_4 \cdot 5H_2O$, 0.5 µM Na_2MoO_3, 0.05 µM $CoCl_2 \cdot 6H_2O$ pH 5.7, with the addition of 10 $g.L^{-1}$ sucrose and 8 $g.L^{-1}$ purified agar). The gametophytes were grown for 4 weeks before transfer to the same medium contaminated with 50 μM of La, Ce, Sm, Gd and Yb. At transfer time, the gametophytes were placed on a cellophane membrane to avoid unintentional REE contamination of the gametophyte blade by the agar medium (only roots were in direct contact with the cellophane membrane). The gametophytes were grown under controlled conditions in a phytotronic chamber (18/23 °C; 8/16 h dark/light cycles; 300 μmol m^{-2} s^{-1}).

Elemental analysis

For the soil $CaCl_2$ extractable fraction, 3 grams of the 2-mm-sieved substrate was dried at 60 °C for 48 h and incubated with 50 mL of 10 mmol L^{-1} calcium chloride under agitation (40 rpm) for 2 h at room temperature. The mixture was first filtered with ash-free filters, subsequently filtered at 0.45 μm and acidified with HNO_3 before inductively coupled plasma-mass spectrometry (ICP-MS) analysis as previously described in Grosjean et al. (2020)[26] using three replicates. A surface water-trace metal standard (SPS-SW1, LGC Prochem standards, United Kingdom) was used as a certified reference material.

For plant sample analysis, fronds were sampled and dried at 60 °C for two days. The ICP-MS quantification of La, Ce, Sm, Gd and Yb was performed from 250 mg of dried powder as previously described in Grosjean et al. (2020)[26] using three biological replicates. Oriental basma tobacco leaves (INCT-OBTL-5, LGC Promochem, Molsheim, France) were used as certified reference material.

Quantification limits (µg. L^{-1}) for the different REEs were: 0.0001 for Pr, Sm, Tb, Tm & Lu; 0.0002 for Ho & Yb; 0.0003 for Sc, Eu, Gd & Er; 0.0004 for Dy; 0.0006 for La, Nd & Y; 0.0008 for Ce.

Photonic microscopy observations

Carmino-green staining was used to identify the vascular tissues in the rachis section. Razor blade cross-sections of approximately 0.5 mm thickness were treated with 12% sodium hypochlorite for 10 min, followed by one wash in water and a second wash in 10% acetic acid. After incubation in the dying mixture (Carmin Vert de Mirande 20180, Sordalab, Etampes, France) for 10 min, sections were thoroughly rinsed in distilled water and observed with a digital light microscope (Keyence - VHX 6000, Bois-Colombes, France). Xylem cells were identified by greenish staining of their lignified walls, whereas cellulosic cell walls, including phloem, were stained pink.

Statistical analysis

ICP-MS data were analyzed statistically by one-way analysis of variance (ANOVA). Normality and homoscedasticity of the data were evaluated and confirmed by Shapiro-Wilks test and Levene's test, respectively. The rejection level was set at $\alpha = 0.05$ in all analyses. Multiple (pair-wise) comparisons between means (n=3) were performed using Tukey's HSD post-hoc test to determine statistical differences. Compact letter display was used as symbolic visualization of significant pairwise comparisons (false discovery rate adjusted p-value (FDR) at the threshold ≤ 0.05).

Table S1. Physico-chemical characteristics of the soil.

Parameter (unit)	Norm	Value
pH_{H2O}	NF ISO 10390	5.6
CEC_{Metson} ($cmol^{+}/kg$)	NF X 31-130	139
Total N (g/kg)	NF ISO 13878	5.64
Organic matter (g/kg)	NF ISO 14235	237
Total organic C (g/kg)	NF ISO 14235	137
C/N		24.2
$P_2O_{5\ (Dyer)}$ (g/kg)	NF X 31-160	0.061
K_2O (g/kg)	NF X 31-108	0.390
MgO (g/kg)	NF X 31-108	0.392
CaO (g/kg)	NF X 31-108	8.30
Na_2O (g/kg)	NF X 31-108	0.040
Fractions (%)	NF31-107	
Clay		46.4
Silt		40.2
Sand		13.4
Rare earth elements	NF X 31-147	
Sum REEs (mg/kg)		217±6
Sc (mg/kg)		3.12±0.10
Y (mg/kg)		13.2±0.6
La (mg/kg)		33.5±1.1
Ce (mg/kg)		115±3
Pr (mg/kg)		7.42±0.21
Nd (mg/kg)		27.4±1.0
Sm (mg/kg)		5.13±0.2
Eu (mg/kg)		0.811±0.03
Gd (mg/kg)		5.43±0.2
Tb (mg/kg)		0.613±0.031
Dy (mg/kg)		2.72±0.11
Ho (mg/kg)		0.505±0.031
Er (mg/kg)		1.32±0.01
Tm (mg/kg)		0.214±0.012
Yb (mg/kg)		1.01±0.04
Ho (mg/kg)		0.101±0.012
Elements ($CaCl_2$ extractible fraction, mg/kg)		
La		0.116±0.024 (0.34% of total La)
Ce		0.349±0.062 (0.3% of total Ce)
Sm		0.022±0.010 (0.43% of total Sm)
Gd		0.026±0.010 (0.48% of total Gd)
Yb		0.0160± 0.008 (1.6 % of total Yb)
Mg		60.6±29.4
Mn		223±85
Na		119±43.1
S		54.6±5.9
Zn		2.07±2.03

Elements concentration values are means ± SE (n=3).

Table S2. REE concentrations in fronds of *Dryopteris erythrosora* grown for 2 months on soils with no REEs added.

Rare earth elements	Value (mg/kg)
La	11.79 ± 5.009
Ce	39.41 ±16.32
Sm	0.998±0.242
Gd	1.059±0.285
Yb	0,433±0.406

REE concentration values are means ± SE (n=3).

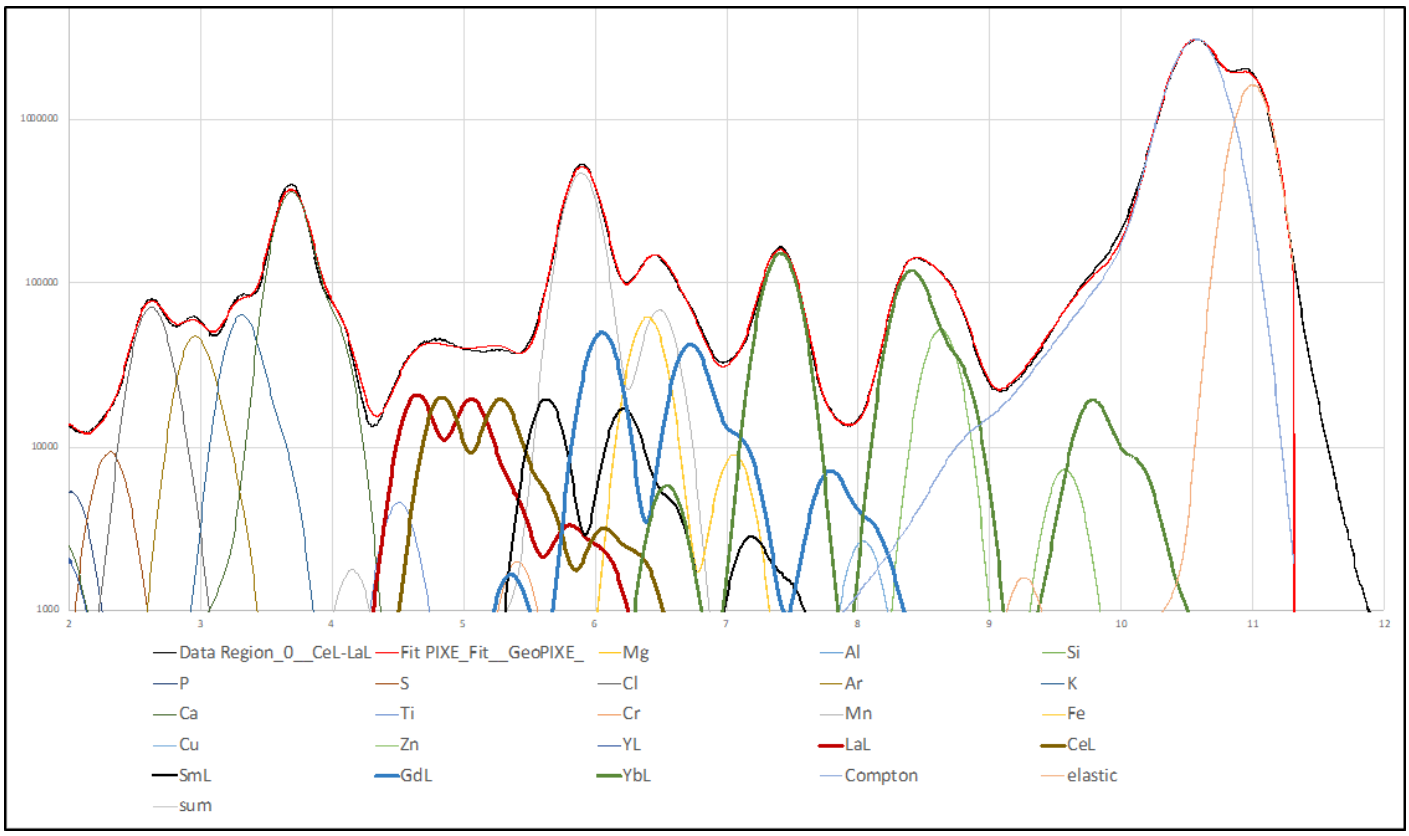

Figure S1. Representative experimental XRF spectrum, fitted spectrum and peak contributions of a *Dryopteris erythrosa* pinnule, collected at 11 keV at P06 beamline.

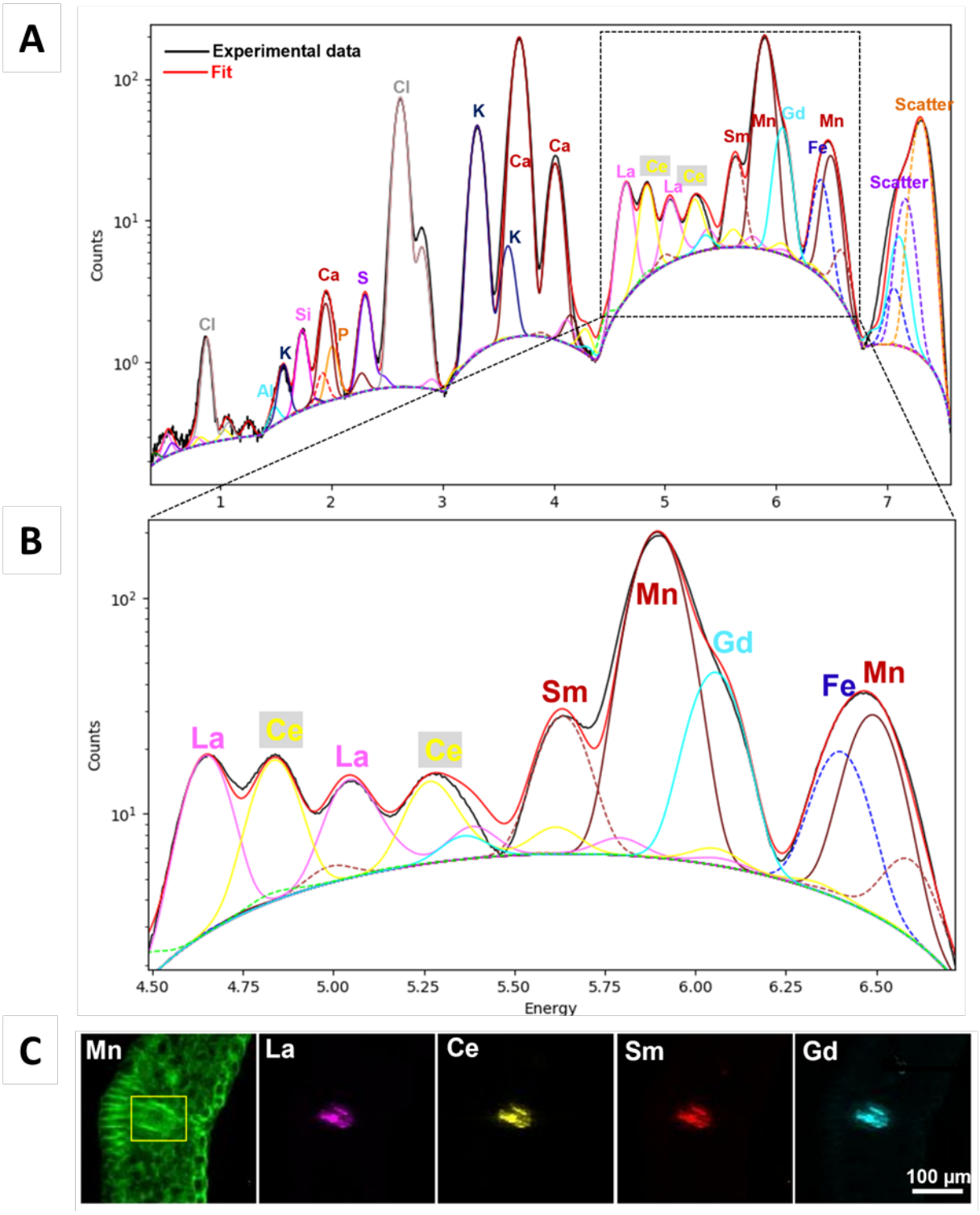

Figure S2. Representative experimental XRF spectrum, fitted spectrum and peak contributions of a *Dryopteris erythrosa* sample, collected at 7.30 keV at LUCIA beamline. A) Whole spectrum acquired from the selected region indicated in C by a yellow square, B) zoom in the 4.50-6.75 keV region and C) resulting XRF maps of Mn, La, Ce, Sm, and Gd.

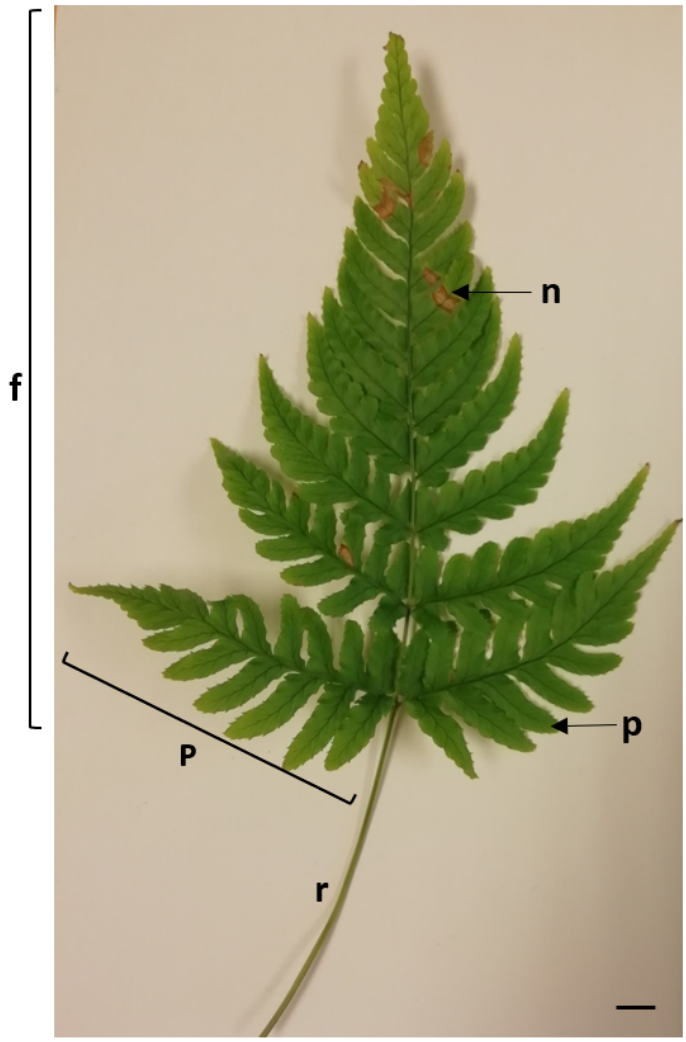

Figure S3. Representative frond of *D. erythrosora* showing the different parts. The scale bar represents 1 cm. Rachis (r), pinna (P), pinnule (p), necrosis (n), frond(f), all the pinnas of the frond constitute the limb.

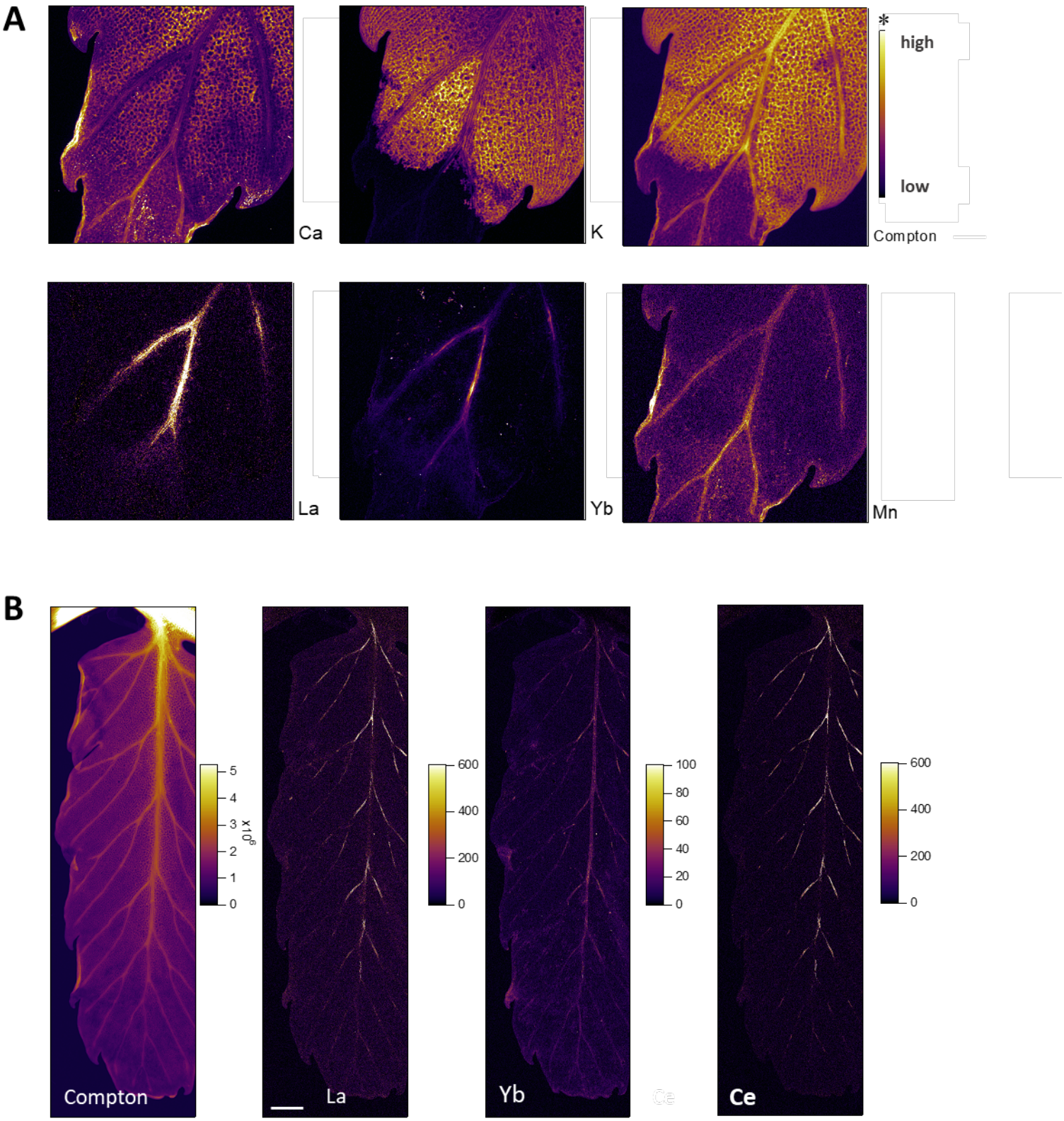

Figure S4. REE distribution in pinnules of *Dryopteris erythrosora* grown under low REE condition (hydroponics) (A) or under medium REE condition (soil culture) (B). X-ray fluorescence elemental maps from fresh *D. erythrosora* pinnules grown hydroponically with 30 µM $LaCl_3$ and 30 µM $YbCl_3$ (A) or in a soil spiked with 83 mg kg^{-1} DW of each REE (B). The images were acquired with a step size of 5 µm (A) or 6 µm (B), with a dwell time of 5 ms (A) or 10 ms (B) per pixel and a 11 keV (A) or 19 keV (B) incident beam. The scale bars represent 30 µm (A) and 800 µm. *For this scan, the low signal/noise ratio prevented a rigorous quantification of elements, so we preferred using a low/high color scale.

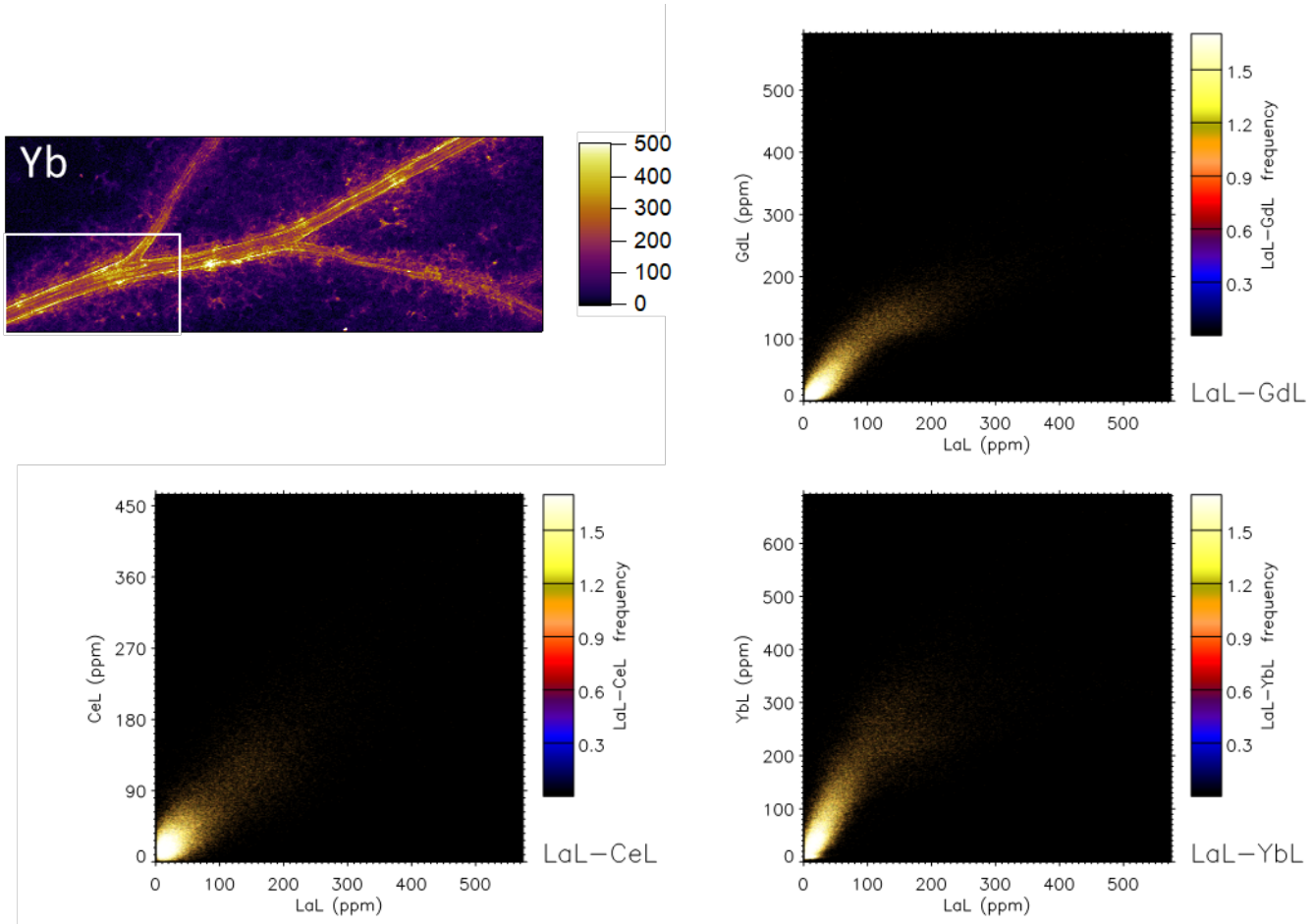

Figure S5. Correlation plots comparing the distribution of REEs in the central vein of pinnules of *Dryopteris erythrosora.* The white box on the Yb map represents the area from which the element plots were drawn.

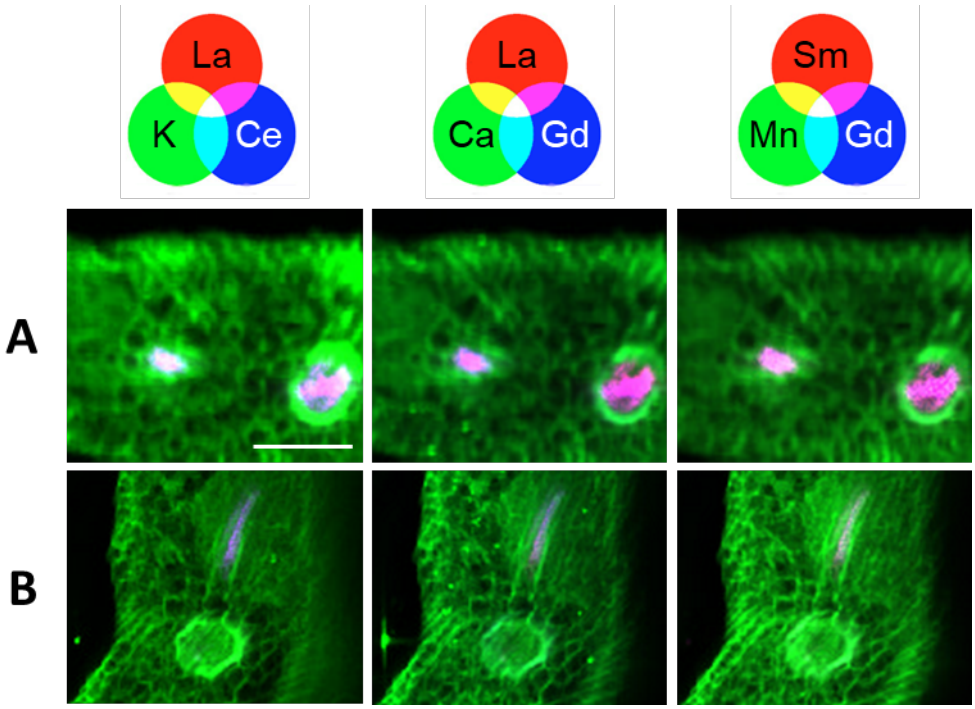

Figure S6. REE distribution inside the vessels of pinnules of *Dryopteris erythrosora*. La-K-Ce (left), La-Ca-Gd (middle) and Sm-Mn-Gd (right) X-ray fluorescence elemental maps were obtained from frozen hydrated cross sections of pinnules of ferns grown on soil supplemented with equal amounts (333 mg kg^{-1} DW each) of La, Ce, Sm, Gd and Yb. The two pinnule sections (A, B) are from independent plants. The images were acquired with a step size of 3 µm, a dwell time of 500 ms per pixel, and the energy of incident beam was set at 7.3 keV. The scale bar represents 100 µm. The color scale is the same for a given element for all samples, including the one shown in Figure 4.

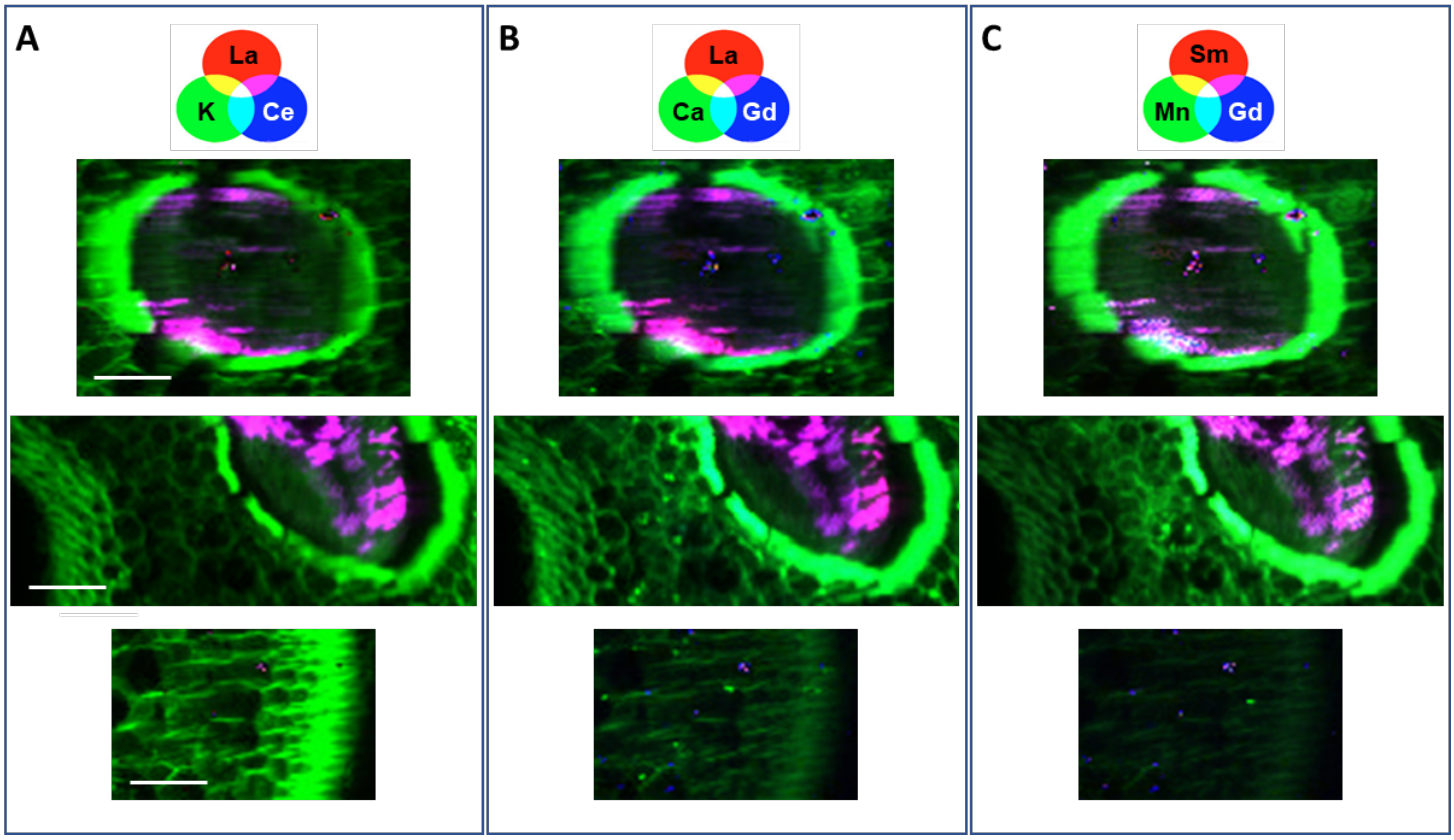

Figure S7. REE distribution in the rachis of *Dryopteris erythrosora*. La-K-Ce (A), La-Ca-Gd (B) and Sm-Mn-Gd (C) X-ray fluorescence elemental maps were obtained from frozen hydrated cross sections of rachis of ferns grown on soil supplemented with equal amounts (333 mg kg-1 DW each) of La, Ce, Sm, Gd and Yb. The images were acquired with a step size of 3 µm, a dwell time of 500 ms per pixel, and the energy of incident beam was set at 7.3 keV. Vascular bundles (upper and middle panels) and epidermis + cortex (lower panel). Middle and lower panels come from the same thin section. The scale bar represents 50 µm. The color scale is the same for a given element for all the samples.

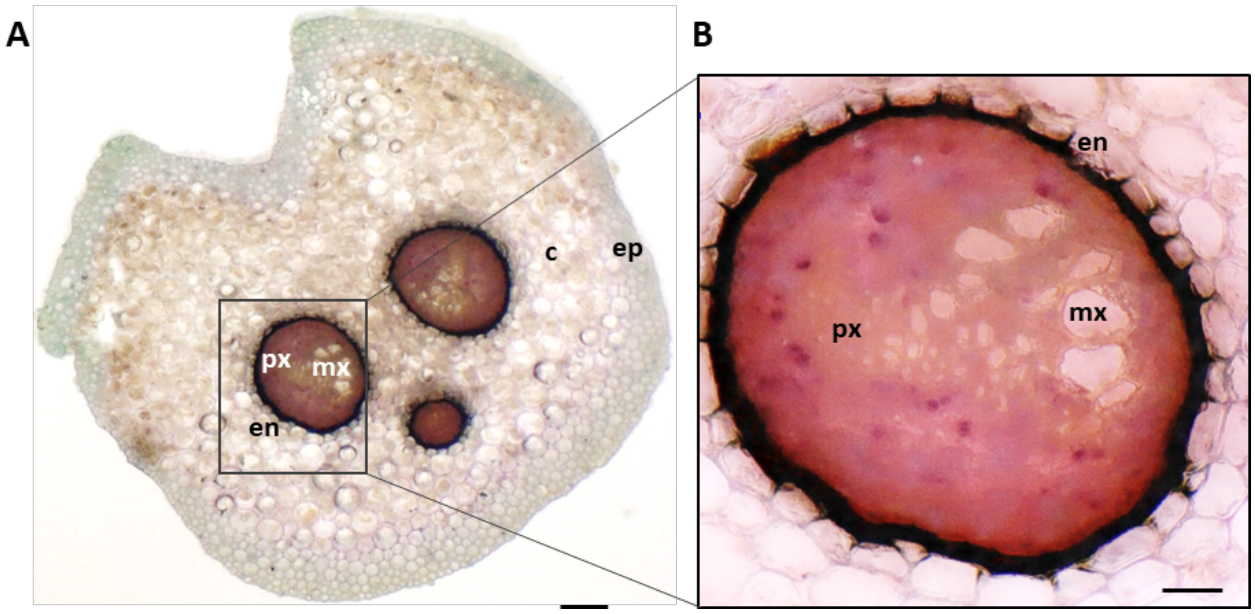

Figure S8. Carmino-green staining of a rachis section (A) with a higher magnification of the stele (B). c: cortex, en: endodermis, ep: epidermis, mx: metaxylem, ph: phloem, px: protoxylem. The scale bar represents 100 µm (A) or 25 µm (B). Representative images are given.

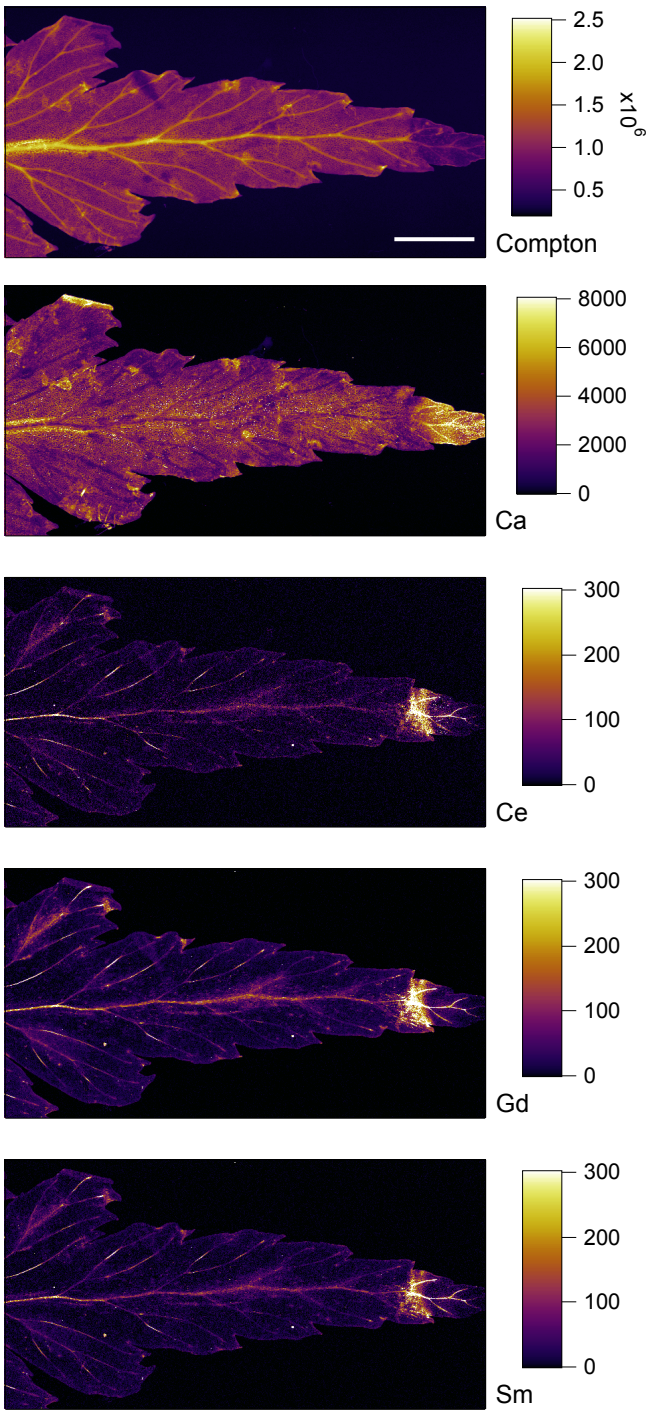

Figure S9. REE distribution and concentrations in the necrotic regions of fronds of *Dryopteris erythrosora*. X-ray fluorescence elemental maps were obtained from fresh pinnae tips of ferns grown on soil supplemented with equal amounts (333 mg kg^{-1} DW each) of La, Ce, Sm, Gd and Yb. The scale bar represents 250 µm.

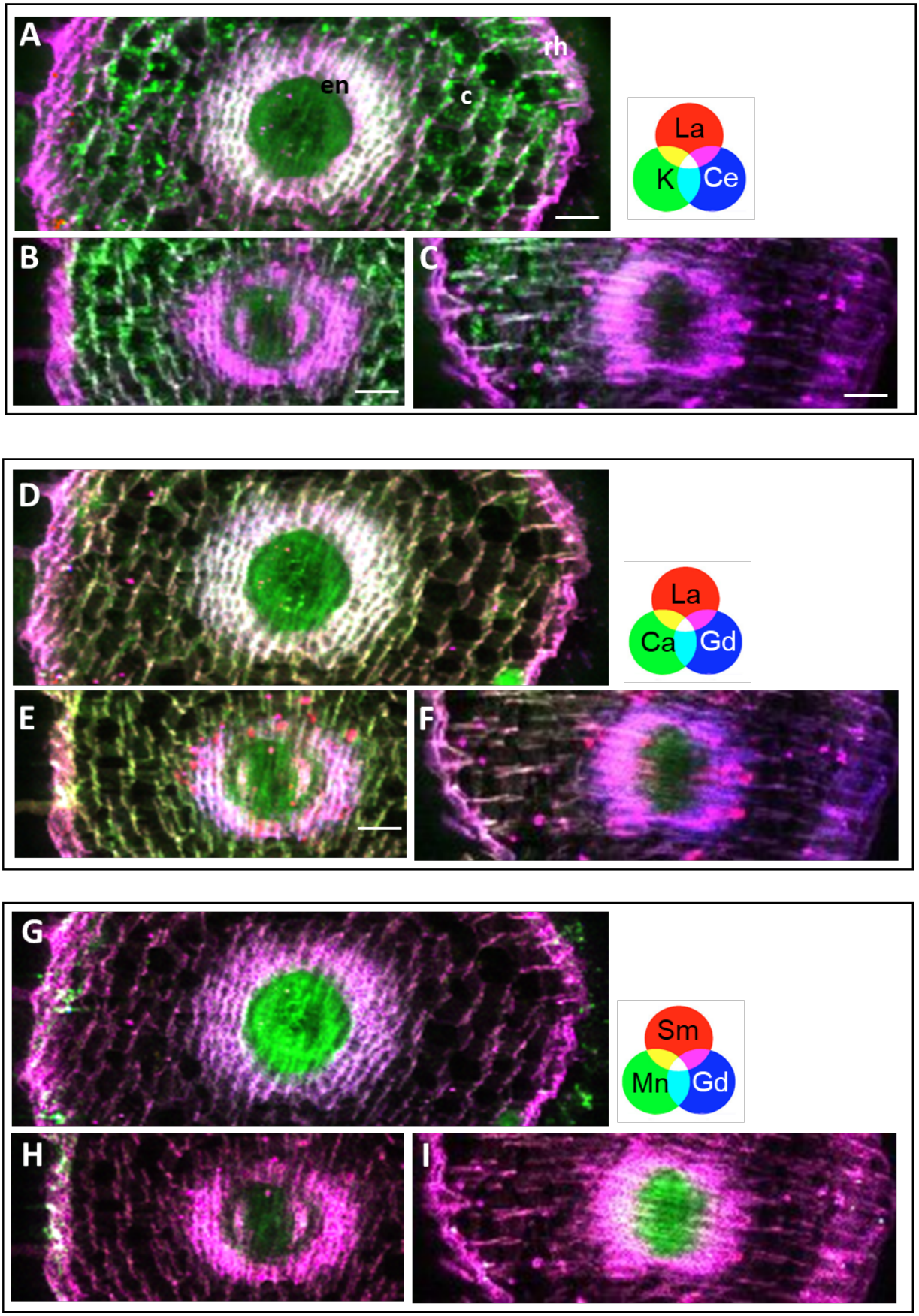

Figure S10. REE distribution in roots of *Dryopteris erythrosora*. X-ray fluorescence elemental maps were obtained from frozen hydrated cross sections of roots of plants grown on soil supplemented with equal amounts (333 mg kg-1 DW each) of La, Ce, Sm, Gd and Yb. (A,D,G) and (B,E,H) are young roots, whereras (C,F,I) is an older root. The images were acquired with a step size of 3 µm, a dwell time of 500 ms per pixel. The scale bar represents 50 µm. Spatial scale and color scale intensity are the same for the three maps. c: cortex, en: endodermis, rh: rhizodermis.

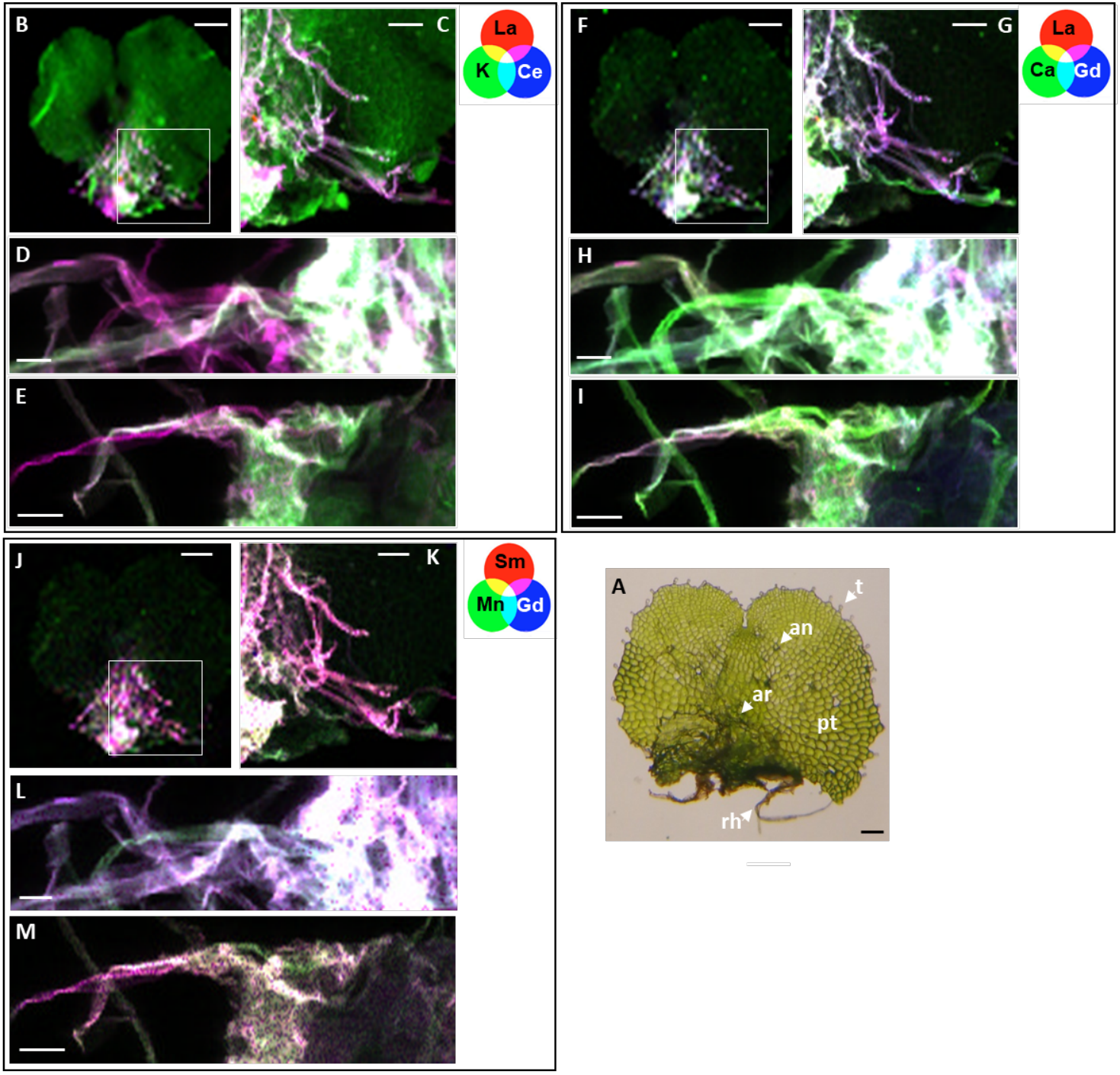

Figure S11. REE distribution in *Dryopteris erythrosora* at the gametophyte stage. (A) shows the anatomy of the *D. erythrosora* gametophyte. an: antheridia, ar: archegonia, pt: photosynthetic tissue, rh: rhizoid, t: trichome. The scale bar in (A) represents 1 mm. La-K-Ce (top left), La-Ca-Gd (top right) and Sm-Mn-Gd (bottom left) X-ray fluorescence elemental maps were obtained from frozen hydrated gametophytes grown *in vitro* and supplemented four weeks with an equimolar mix of five REEs. (B,F,J) represents the whole gametophyte and (C,G,K) are higher resolution scans of the area depicted in (B,F,J) which corresponds to the base of the gametophyte with rhizoids. (D,H,L) and (E,I,M) are rhizoids from two other gametophytes. The images were acquired with a step size of 50 µm (B,F,J), 12 µm (C,G,K) or 3 µm (D,H,L and E,I,M) with a dwell time of 100 ms (B,F,J) or 500 ms (other panels) per pixel and the energy of the incident beam was set at 7,3 keV. The scale bars represent 500 µm (B,F,J), 200 µm (C,G,K) or 50 µm (D-E, H-I, L-M). The color scale is the same for a given element for all the samples.